The Structural Dynamics of Force Generation in Muscle, Probed by Electron Paramagnetic Resonance of Bifunctionally Labeled Myosin

A DISSERTATION
SUBMITTED TO THE FACULTY OF THE GRADUATE SCHOOL
OF THE UNIVERSITY OF MINNESOTA
BY

Andrew Russell Thompson

IN PARTIAL FULFILLMENT OF THE REQUIREMENTS
FOR THE DEGREE OF
DOCTOR OF PHILOSOPHY

David D. Thomas

May 2009

© Andrew Russell Thompson 2009

Acknowledgements

This project and my graduate career were possible because of the continued support of **David Thomas.** Dave was kind enough to let a poor starving physicist into his lab and taught me that biology was more complicated and interesting than cutting open fetal pigs. He has been an excellent mentor in science, life and, of course, wine.

My friendships with **David Kast** and **Sarah Blakely** have been absolutely invaluable. Dave is responsible for me coming to the University of Minnesota, due to his continued willingness to have a good time. Sarah has been a very close friend, and has always been there to answer my stupid questions about buffers and pH. Both of you I will be very sad to leave!

None of this work would have gotten done without the aid of my friends **Christina Yi** and **Eunice Song**. Despite my best attempts to reform, I am still a physicist at heart, and without their help I would have never had protein to study. Special thanks to Christina, who was almost always willing to make me some buffers and tie a few fibers.

I have enjoyed my work with **Ryan Mello** and **Roman Agafonov.** Roman has forced me to become a better scientist, with his constant question of "Why?!" Ryan and I have spent countless hours breaking muscle fibers, pipetting in the dark and building equipment out of duct tape and tubing.

Thank you to **Octavian Cornea,** for the constant help with making posters and getting Microsoft products to behave properly.

Finally, thank you to all of my family for supporting me during my education, without you I never would have made it this far!

Dedication

To my family,

who have always supported me.

and

To my wife,

for pushing me to finish this.

Abstract

Two proteins in muscle, actin and myosin, are the key structural components that interact in order to produce muscle contraction. Myosin is a molecular motor that utilizes the chemical energy of ATP to undergo conformational changes that translate actin linearly, resulting in mechanical work. While previous studies have provided high-resolution measurement of these structural changes, many are unable to do so in intact muscle or in systems where myosin and actin can interact.

This project seeks to make high-resolution structural measurements of myosin in actomyosin complexes during the different biochemical states associated with contraction. These measurements are being made using electron paramagnetic resonance (EPR), a spectroscopic technique sensitive to protein dynamics and orientation. In order to study myosin with EPR, a spin label is chemically attached to cysteine within the protein structure. In certain cases, native cysteines are used for spin labeling whereas in others, mutant protein is created with cysteines engineered in desired locations, a process known as site-directed spin labeling.

Traditional spin probes attach via a single, flexible bond. This monofunctional attachment limits the sensitivity of EPR to protein orientation and dynamics because the resultant spectra are a mixture of probe and protein states. This project, on the other hand, uses a novel bifunctional spin label that is rigidly coupled to the protein via attachment to two engineered cysteines. Due to this rigid coupling, high-resolution structural measurements can be made with a degree of sensitivity not available to other techniques.

Table of Contents

List of Tables

List of Figures

Alphabetical List of Abbreviations

A, actin
ADP, adenosine diphosphate
AlF_4, aluminum fluoride
ATP, adenosine triphosphate
BSL, bifunctional spin label
D, ADP
Dicty, *Dictyostelium discoideum*
Dicty S1dC, *Dictyostelium discoideum* myosin II motor domain
EPR, electron paramagnetic resonance
L50kD, lower 50 kilo-Dalton (domain)
NASA, place that rejected my astronaut application
NS, non-specific (binding)
P, phosphate
S, strong binding state
S1, subfragment 1
sBSL, saturated BSL
SH1, sulfhydryl 1
SH2, sulfhydryl 2
STEPR, saturation transfer EPR
T, ATP
U50kD, upper 50 kilo-Dalton (domain)
uBSL, unsaturated BSL
V, vanadate
W, weak binding state
WS, weak-strong binding state
WT, wild-type

Chapter 1 - Introduction to Muscle

1.1. Introduction

The principle proteins of muscle, myosin and actin, utilize the chemical energy of ATP to produce mechanical work, and thus muscle contraction. Myosin II, the type of myosin found in muscle, is part of a larger family of molecular motors (myosins, kinesin and dynein), that share many structural, biochemical and mechanical similarities. Because of this, muscle plays a central role in basic biophysical research, providing a testing ground for fundamental hypotheses in cellular movement, and it allows us to

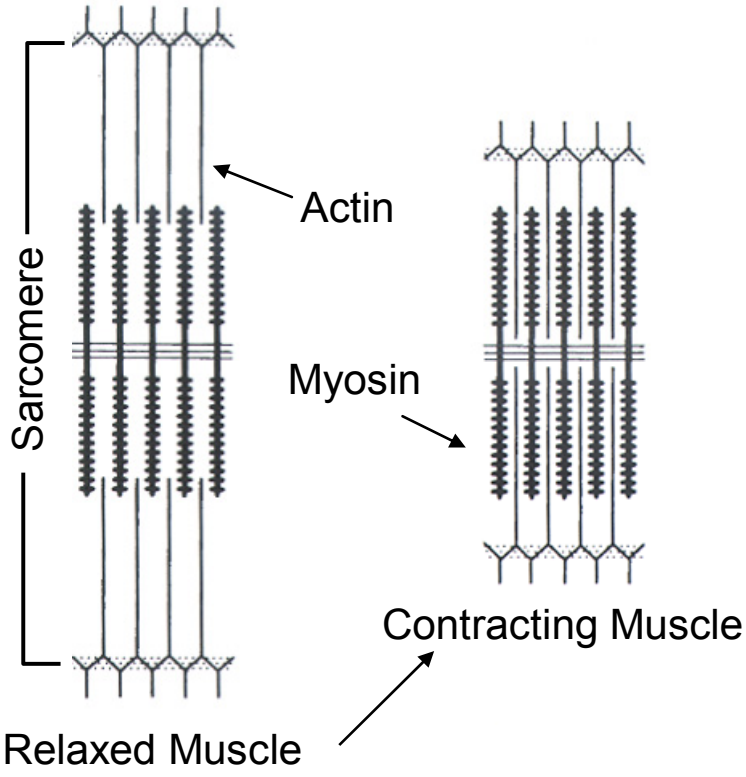

Fig. 1: The sarcomere
A schematic of the fundamental unit of muscle contraction. The sarcomere is composed of interdigitating thick (barbed lines) and thin (narrow lines) filaments which are comprised of myosin and actin respectively. Adapted from (1).

study how myosin dysfunction results in major medical problems, such as heart disease and aging.

The fundamental subunit of muscle is the sarcomere, which is composed of interdigitating thick and thin filaments (**Fig. 1**). Contraction is accomplished by the relative motion of the thick and thin filaments, also known as the sliding filament theory (3). The dominant protein of the thin filament is actin, a globular protein with a molecular weight of 42kD that polymerizes into a helical filament called F-Actin with a 37 nm periodicity. The thick filament is composed of myosin, a dimeric molecular motor of molecular weight nearly 500 kD, containing two 120 kD heads, joined by long α -helical tails in the form of a coiled-coil (**Fig. 2**). Thick filament formation occurs by the bundling of myosin tails.

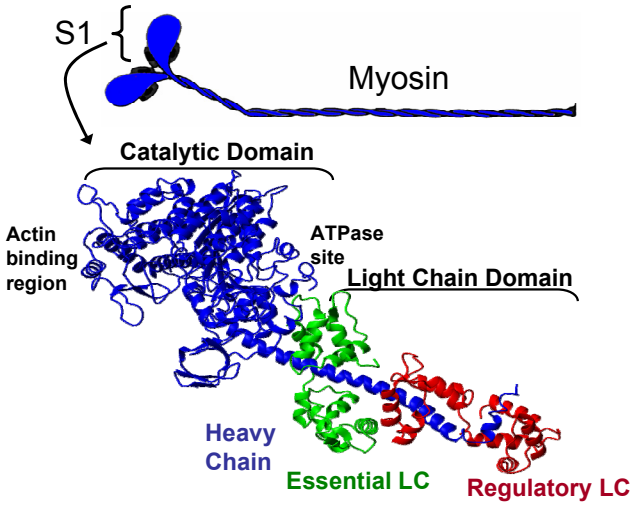

Fig. 2: Myosin
The cartoon illustrates myosin's long coiled-coil tail and globular head region. The functional domain of myosin (S1) is represented as a crystal structure (2). The catalytic domain (blue) contains the actin binding region and site for ATP hydrolysis. The catalytic domain extends to the light chain domain, comprised of the essential light chain (green) and the regulatory light chain (red).

The head region of myosin (S1) contains all of the functional domains of the molecular motor. The catalytic domain contains an actin binding domain and a site for ATP hydrolysis. The light chain domain is an extension of the catalytic domain and is stabilized by two light chains, the essential light chain and the regulatory light chain. The light chain domain is one of the key elements that undergoes conformational changes during muscle contraction, undergoing rotation and acting as a lever arm (7). The catalytic domain itself is composed of a series of specialized "organs" which facilitate actin binding, hydrolysis of ATP, transmission of mechanochemical information and the rotation of the lever arm (**Fig. 3**).

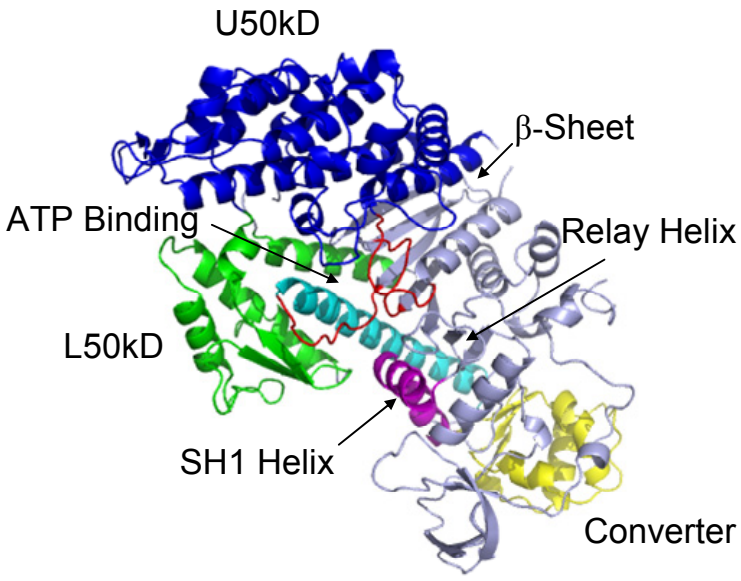

Fig. 3: Organs of the catalytic domain.
Crystal structure of Dicty S1dC in rigor (1FMV, (4)).The U50kD domain (blue) and L50kD domain (green) play a role in actin binding (5). The ATP bind site (red) facilitates nucleotide binding and hydrolysis. The relay helix (cyan) and the SH1 helix (magenta) transmit information from the nucleotide binding site to the Converter (yellow) which rotates the light chain domain (6). The β-sheet acts as a hinge between the U50kD and L50kD domains (5).

1.2 Actin-Myosin Interaction: The Crossbridge Cycle

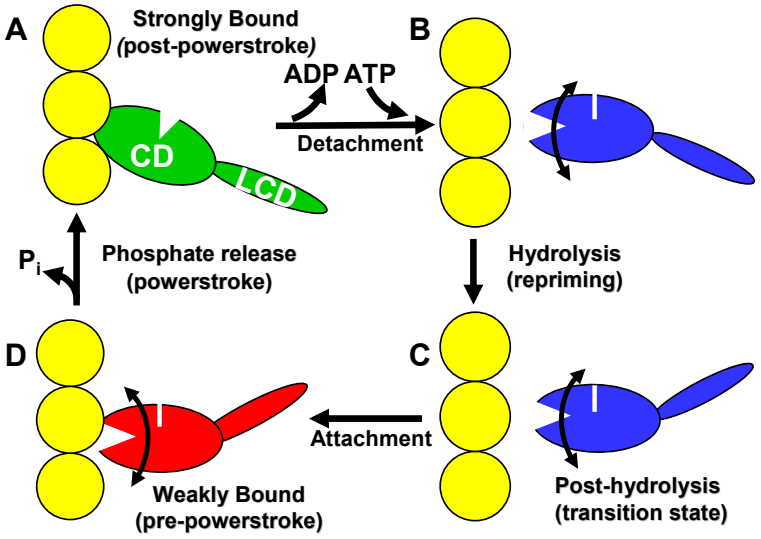

Fig. 4: The actomyosin ATPase.
Actin and myosin interact, utilizing ATP to produce a power stroke. Green represents strong binding states. Red represents primarily attached weak binding states. Blue signifies primarily detached weak binding states. Arrows signify orientational disorder and faster dynamics. Adapted from (8).

The cyclic interaction of actin and myosin is responsible for muscle contraction (**Fig. 4**). Myosin is an enzyme that facilitates the hydrolysis of ATP, the chemical fuel source used by most organisms. However, the rate at which myosin hydrolyzes ATP in the absence of actin is slow. In the presence of actin, myosin's rate of ATPase is greatly increased and becomes a biologically relevant machine for ATP hydrolysis. In the absence of nucleotide (rigor) or presence of ADP, myosin will bind actin to form a rigidly bound complex (**Fig. 4** A). Upon ATP binding, myosin dissociates from actin where it converts ATP to ADP.P_i, and the lever arm is re-primed to a pre-powerstroke orientation (**Fig. 4** B-C). Once hydrolysis of ATP has occurred, myosin forms a weak binding complex with actin (**Fig. 4** C-D). Upon the release of phosphate, myosin undergoes a

disorder to order transition, forming a strong binding state with actin, accompanied by a rotation of the lever arm and displacement of actin (**Fig. 4** D-A). Spectroscopic evidence suggests that the disorder to order transition, along with ADP release is the source of force generation and therefore work in the form of contraction (7).

1.3. Lingering Questions, a Need for Spectroscopy

Despite the compelling schematic for muscle contraction, much about the mechanism of actomyosin interaction and force generation is not well understood. In fact, all of the high resolution crystal structures of myosin were obtained in the absence of actin. The simple observation that myosin ATPase is accelerated by actin suggests that there is more to the story than the isolated structure of myosin, necessitating the need for high resolution structures of myosin while bound to actin *in vitro*.

Spectroscopy, particularly electron paramagnetic resonance (EPR), is an ideal methodology for the study of muscle because it can yield information about protein orientation and dynamics at the molecular level in conditions that are similar to those found *in vivo*. With the advent of site-directed mutagenesis, it is now possible to engineer cysteines at specific residues which can be labeled with cysteine specific probes. The following chapters will illustrate the power of EPR for making high resolution structural measurements of myosin in the presence of actin, in order to elucidate the mechanism of force generation.

Chapter 2 – Introduction to Electron Paramagnetic Resonance

2.1. The Zeeman Effect

The Stern-Gerlach experiment demonstrated that an electron possessed an intrinsic amount of angular momentum called spin. It was originally conjectured that the electron spun about its axis, generating a magnetic dipole parallel to this intrinsic angular momentum. This model, while useful for illustration purposes, is entirely incorrect as the electron has no classical structure.

In the presence of an external magnetic field $\mathbf{B_0}$, the energy of an unpaired electron (U) will be a projection of the electron's magnetic moment on the field, at a minimum when they are in alignment:

$$U = -\boldsymbol{\mu} \bullet \mathbf{B_0} = -|\mu B_0| \cos(\theta_{\mu B}) \tag{1}$$

where μ is the magnetic moment and $\theta_{\mu B}$ is the angle between $\boldsymbol{\mu}$ and $\mathbf{B_0}$. In the notation of Quantum Mechanics, the corresponding Hamiltonian ($\mathcal{H}$) would be:

$$\mathcal{H} = -\mathbf{B_0} \bullet \boldsymbol{\mu} = g_e \beta_e \mathbf{B_0} \bullet \hat{\mathbf{S}} \tag{2}$$

with β_e representing the electron Bohr magneton, g_e is a constant and $\hat{\mathbf{S}}$ is the spin operator. If we arbitrarily choose the magnetic field to be along the z axis, the Hamiltonian is reduced to:

$$\mathcal{H} = g_e \beta_e B_0 S_z \tag{3}$$

and we can measure the energy of an electron spin state $|m_s = \pm 1/2>$ by acting on it with this Hamiltonian. Thus, the energy is given as:

$$U_{ms} = < m_s = \pm 1/2|\mathcal{H}\,|\, m_s = \pm 1/2> \tag{4}$$

$$= \pm \frac{1}{2} g_e \beta_e B_0$$

The energy between these two states is merely:

$$\Delta U = g_e \beta_e B_0 \tag{5}$$

In the presence of a source of photons (energy), an electron in the ground state can absorb energy and be put into an exited state when the energy of the photon is equal to the energy gap ΔU (Fig. 5).

$$h\nu = g_e \beta_e B_0 \tag{6}$$

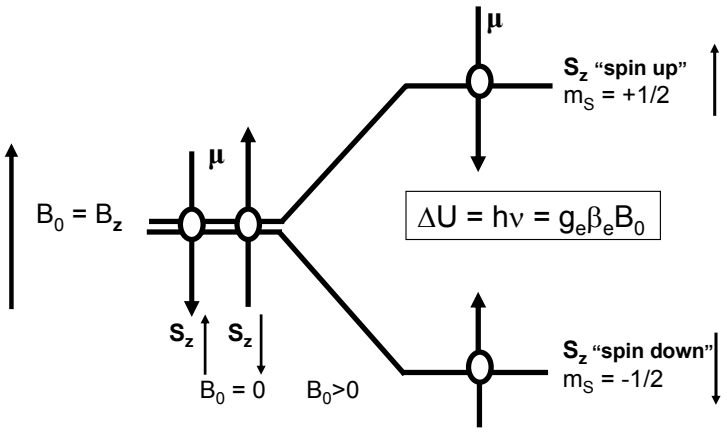

Fig. 5: The Zeeman Effect
Electron energy level splitting due to the Zeeman Effect. Adapted from (9).

Here, the energy of the photon is given by Planck's constant (h) times the frequency (ν) of the light. This is electron paramagnetic resonance.

2.2. The EPR Spectrometer

The absorption of a photon by the electron is what is measured by an EPR spectrometer (Fig. 6 A). The spectrometer, on the simplest level, consists of a source for

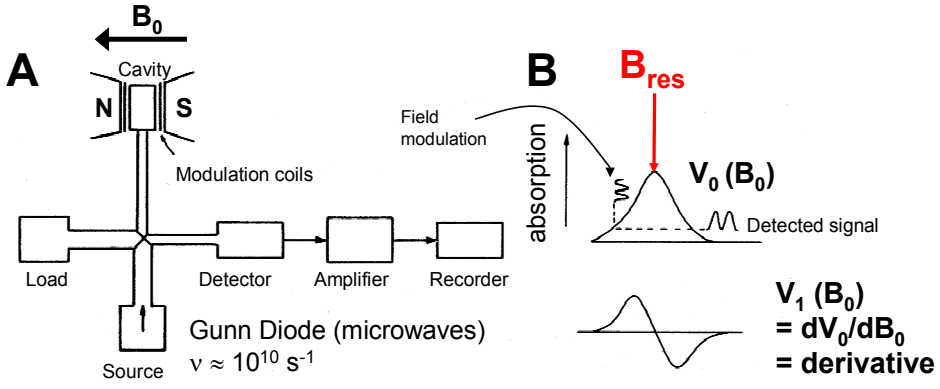

Fig. 6: The EPR spectrometer
(A) A simple EPR spectrometer. (B) The effect of field modulation on the signal. Adapted from (9)

photons (microwaves), a magnet, a resonant cavity (for the sample) and a detector. There are two ways of creating the transition shown in Fig. 5, either by varying the frequency (ν) of the microwaves or by varying the magnetic field ($\mathbf{B_0}$) generated by the magnet. The latter is chosen, as it is easier to vary the current in the electromagnet, and thus the magnetic field, than it is to vary the source of microwaves. For a given frequency (9.5 GHz for X-band EPR) of microwaves, the magnetic field is swept until the resonance condition:

$$B_{res} = \frac{h\nu}{g_e \beta_e} \tag{7}$$

is met and absorption of a photon by an electron will occur. To facilitate a good signal to noise ratio, the magnetic field is given a sinusoidal 100 kHz modulation. Therefore, rather than the output of absorption vs. field (V_0), the derivative of the absorption vs. field (V_1) is observed (Fig. 6 B).

2.3. g Anisotropy

Though the electron is in the presence of an external field, local fields may be present (such as those generated by nearby matter) that perturb the field experienced by the electron, resulting in an effective magnetic field in the neighborhood of the electron ($\mathbf{B_{eff}}$):

$$\mathbf{B_{eff}} = \mathbf{B_0} + \mathbf{B_{local}} \tag{8}$$

Thus Hamiltonian becomes:

$$\mathcal{H} = g_e \beta_e \mathbf{B_{eff}} \cdot \hat{\mathbf{S}} \tag{9}$$

Since we cannot measure the local field directly, we would like to write our equations in terms of the lab generated field. It is safe to assume that the local field is proportional to $\mathbf{B_0}$, as the source of the local field is likely due to other nearby magnetic centers. Thus, we can write the rewrite the Hamiltonian:

$$\mathcal{H} = g_e \beta_e (1-s)\, \mathbf{B_0} \cdot \hat{\mathbf{S}} = g\, \beta_e\, \mathbf{B_0} \cdot \hat{\mathbf{S}} \tag{10}$$

This new g factor is likely anisotropic, and will be dependent upon its orientation to the applied magnetic field. It is mathematically convenient then, to represent the Hamiltonian in matrix form:

$$\mathcal{H} = \beta_e \mathbf{B_0} \bullet \mathbf{g} \bullet \hat{\mathbf{S}} \tag{11}$$

and the matrix values can be determined from experiment. Once these values are obtained, the principle axes of the spin system can be found. Alternatively, we can write **g** in terms of the angles θ and φ between the magnetic field and the principle axes of the spin system. This formulation:

$$g(\theta,\varphi) = g_x \sin^2\theta\cos^2\varphi + g_y \sin^2\theta\sin^2\varphi + g_z \cos^2\theta \tag{12}$$

allows for a more useful representation of the anisotropic resonance condition

$$B_{res} = \frac{h\nu}{g(\theta,\varphi)\beta_e} \tag{13}$$

2.4 Nuclear Hyperfine Interaction

In the presence of a nearby nucleus, the energy states of the unpaired electron are split due to the hyperfine interaction. The cause of this splitting is due to a perturbation of the field at the electron generated by the dipolar field of the nucleus. Each Zeeman absorption line will be split into (2I+1) lines of equal magnitude, where I is the spin of the nucleus. In the presence of n identical nuclei, the number of lines will be (2nI+1) and the relative intensity of each resonance peak will follow the binomial expansion.

For all orbitals above s, the electron cloud about the nucleus is not spherically symmetric. Since the dipolar field of the nucleus depends on not only distance but also on

angular distribution, this gives rise to anisotropy in the hyperfine interaction. Similar to the anisotropy in the Zeeman interaction, it is useful to represent the hyperfine anisotropic interaction in spherical-polar form:

$$A(\theta,\varphi) = (A_x^2\sin^2\theta\cos^2\varphi+A_y^2\sin^2\theta\sin^2\varphi+A_z^2\cos^2\theta)^{1/2} \quad (14)$$

and the resonant field becomes:

$$B_{res}= \frac{h\nu - m_I\, A(\theta,\varphi)}{g(\theta,\varphi)\beta_e} \quad (15)$$

$$= \frac{h\nu}{g(\theta,\varphi)\beta_e} - m_I\, T(\theta,\varphi)$$

where m_I is the nuclear quantum number and $T(\theta,\varphi)$ has units of magnetic flux density. Similar to g, the components of T need to be found through experiment.

Equation 15 suggests that each resonance is uniquely defined for a single value of θ,φ. Since these are quantum mechanical systems, though, the Heisenberg Uncertainty Principle is experimentally relevant and imparts a non-trivial width to each absorption line. The width of this line is proportional to the rate of relaxation from the exited state to the ground state. The Bloch equations, which predict the classical magnetization of a system, yield a line shape due to this broadening will be Lorentzian. Hence, the observed spectrum will be that of first derivative Lorentzians centered about the resonance fields B_{res} given by Equation 15.

For EPR to be useful in the study of biological systems, we need to introduce a free radical into a system and have it remain stable. Nitroxide spin labels are one solution to this problem. Though they come in a variety of forms to facilitate binding needs, the common thread is that they have a nitroxide with a single unpaired electron in a p-type orbital about the nitrogen atom. Since the nitrogen nucleus is a spin one particle, this gives rise to a 3 line spectrum (**Fig. 7**).

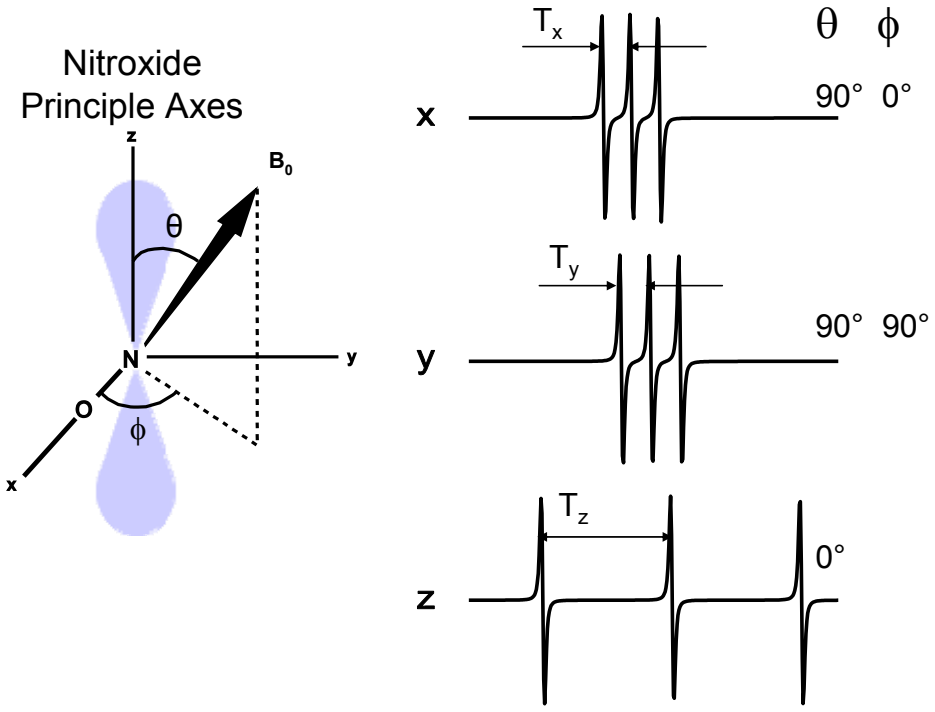

Fig. 7: Hyperfine anisotropy
Nitroxide spectra for the external field (B_0) along the Nitroxide principle axes. The shift in center resonance is due to g anisotropy.

2.5. Dynamics and Orientation

It is clear from **Fig. 7** that a spin system that is sensitive to orientation would be ideal in understanding protein configuration, but such specific orientations are often not what are observed. Two separate effects, orientational distribution and dynamics, must be considered in understanding experimental spectra.

The spectrum for a large orientational distribution of completely immobilized spin labels, whose absorption spectra will be that of Lorentzians centered about the resonance fields given by Equation 15, can be calculated by making a linear combination of the spectra for each given orientation. Given an orientation distribution function $\rho(\theta,\varphi)$, typically Gaussian, one can compute the spectrum one will observe via the convolution:

$$V_1(B) = \int V_i(B,\theta,\varphi)\rho(\theta,\varphi)\sin(\theta)d(\theta,\varphi) \tag{16}$$

The effect of dynamics on a system is less simplistic in appearance. The easiest regime to understand is fast isotropic motion (sub nanosecond). Here all the anisotropies in g and T are averaged out:

$$g_0 = \frac{1}{3}(g_x + g_y + g_z) \tag{17}$$

$$T_0 = \frac{1}{3}(T_x + T_y + T_z)$$

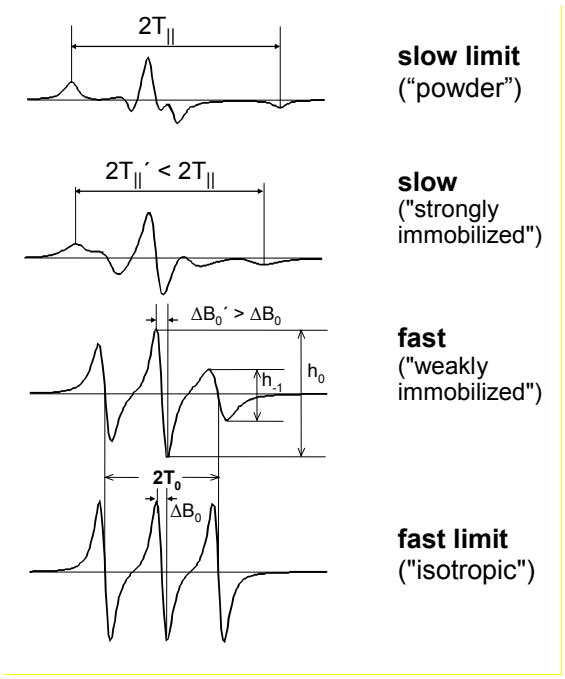

Fig. 8: Isotropic nitroxide tumbling
The effect of isotropic tumbling on a Nitroxide spectrum

The spectrum given by the above values is observed for free spin labels tumbling in a low viscosity solution. For motions that are slower than rapid isotropic tumbling (10^{-9}–10^{-7}s), the effect of isotropic tumbling on spectral features is twofold. The first effect is averaging of the orientational effects of g and T, though not to the magnitude of the rapid isotropic motion case. The second effect is a broadening of the line width. As the field is swept, the motion of the spin label moves on and off resonance, which can be perceived as an enhancement of relaxation. As the rate of relaxation is coupled to line width, slow tumbling motions will broaden out the line. Here it is useful to note that to a good approximation, the T of the Nitroxide has azimuthal symmetry with $T_{||} = T_z$ and $T_{\perp} = T_x = T_y$. With this approximation, the measurement of spectral features and the use of the stochastic Liouville simulations of a sphere tumbling in solution, an estimate of the rotational correlation time can be obtained (Fig. 8).

For a strongly immobilized spin label, the low and high field peaks are well resolved and can be used to measure the rotational correlation time τ_r using a comparison to the rigid limit.

$$\tau_r = a[1-(T_{\parallel}'/T_{\parallel})]^b \quad (18)$$

For labels that are weakly imobilized, spectral features must be compaired to that of the isotropic limit

$$\tau_r = z \bullet \Delta B_0' [(h_0/h_{-1})^{1/2}-1] \quad (19)$$

Here the values for a, b, and z are $5.4 * 10^{-10}$s, -1.36 and $1.15*10^{-8}$s respectively (from simulation), and the unprimed value for $T_{\parallel}$ should be found from the frozen (rigid limit) spectrum.

In the case of anisotropic tumbling (Fig. 9) it is useful to describe the amount of motion with the order parameter S, which is merely the ratio of the observed anisotropy ($T'_{\parallel} - T_0$) with the maximum anisotropy ($T_{\parallel} - T_0$). This can be used to calculate the time averaged amount of angular variation ($\Delta\theta$):

$$S = \frac{T'_{\parallel} - T_0}{T_{\parallel} - T_0} = \frac{1}{2}(3\langle\cos^2\Delta\theta\rangle - 1) \qquad (20)$$

In the regime of slower molecular tumbling (10^{-7}–10^{-3}s), conventional EPR is insufficient in resolving differences in dynamics. Often this is the time scale that is relevant to many of the motions of protein domains, including myosin. A different technique, saturation transfer EPR (STEPR) can be used to measure dynamics. This technique will be covered in more detail in CHAPTER 4.

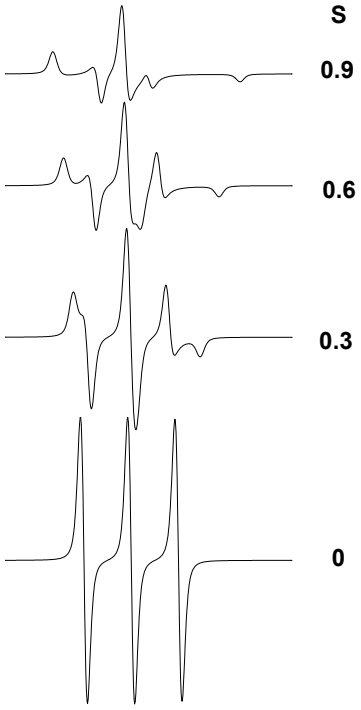

Fig. 9: Anisotropic spin label tumbling
Order parameters for a spin label with anisotropic tumbling (10^{-11}s)

Chapter 3 – The Bifunctional Spin Label

3.1 Bifunctional vs. Monofunctional Spin Labeling

Traditional nitroxide spin labels attach to the protein through a single, often flexible chemical bond. To effectively study the orientation and dynamics of a protein using spectral features, one must be confident that the information is representative of the protein's behavior and not merely due to flexibility in the spin label's attachment. This can be accomplished by using a spin label that bifunctionally binds to an α-helical region on a protein, which has a periodicity of 3.6 residues per helix turn. By fixing this bifunctional spin label (BSL) to a protein that has been modified to have cysteines at residue i and i+4 (or in some cases i and i+3), you achieve a spin label that is rigidly coupled to the helix and is a more accurate reporter of protein dynamics and orientation (**Fig. 10**).

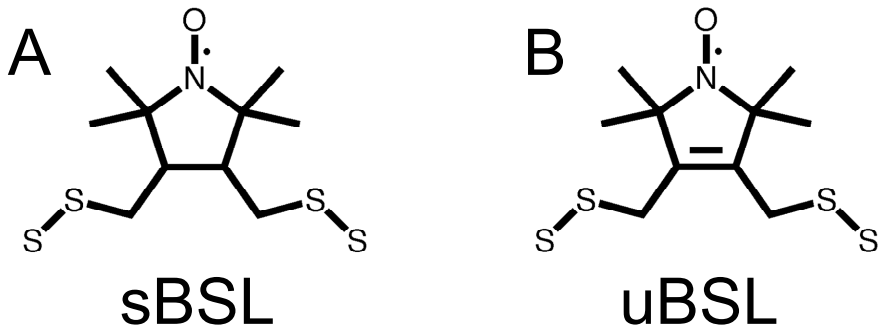

Fig. 10: Bifunctional spin labels
(A) Saturated bifunctional spin label. (B) Unsaturated bifunctional spin label.

Two commercially available bifunctional spin labels were employed in these studies: saturated BSL (sBSL, **Fig. 10** A.) and unsaturated BSL (uBSL, **Fig. 10** B). Both spin labels have identical cysteine linker length but differ by a double bond found in the unsaturated BSL nitroxide ring. This extra bond increases the stability of the nitroxide ring, forcing planar geometry and therefore a consistent spin label orientation. The saturated BSL ring, on the other hand, has conformational flexibility in the ring structure, introducing a spread of nitroxide vector orientations. While this reduces the effectiveness of sBSL as a probe of orientation, its rigid coupling to the protein backbone still limits spin label dynamics and is therefore an effective reporter of protein motion.

3.3. BSL Helix Conformations

A study of X-ray scattering on uBSL labeled crystallized T4 Lysozyme found that the spin label had a well resolved electron density and that the normal of the nitroxide ring, and thus the spin label principle axis, was perpendicular to the axis of the labeled helix (10). The spectrum of uBSL labeled at residues A639C.A643C of *Dictyostelium discoideum* myosin S1 bound to actin (presented in further detail in CHAPTER 5), in contrast, reveals two distinct spin label conformations with respect to the helix axis (**Fig. 11**). The structure presented in (**Fig. 11** A) is in good agreement with the observed orientation in the T4 Lysozyme crystal structure. The fact that (**Fig. 11** B) was not resolved in the crystal suggests that this orientation of the spin label, and its probability, is sensitive to the choice of labeling sites.

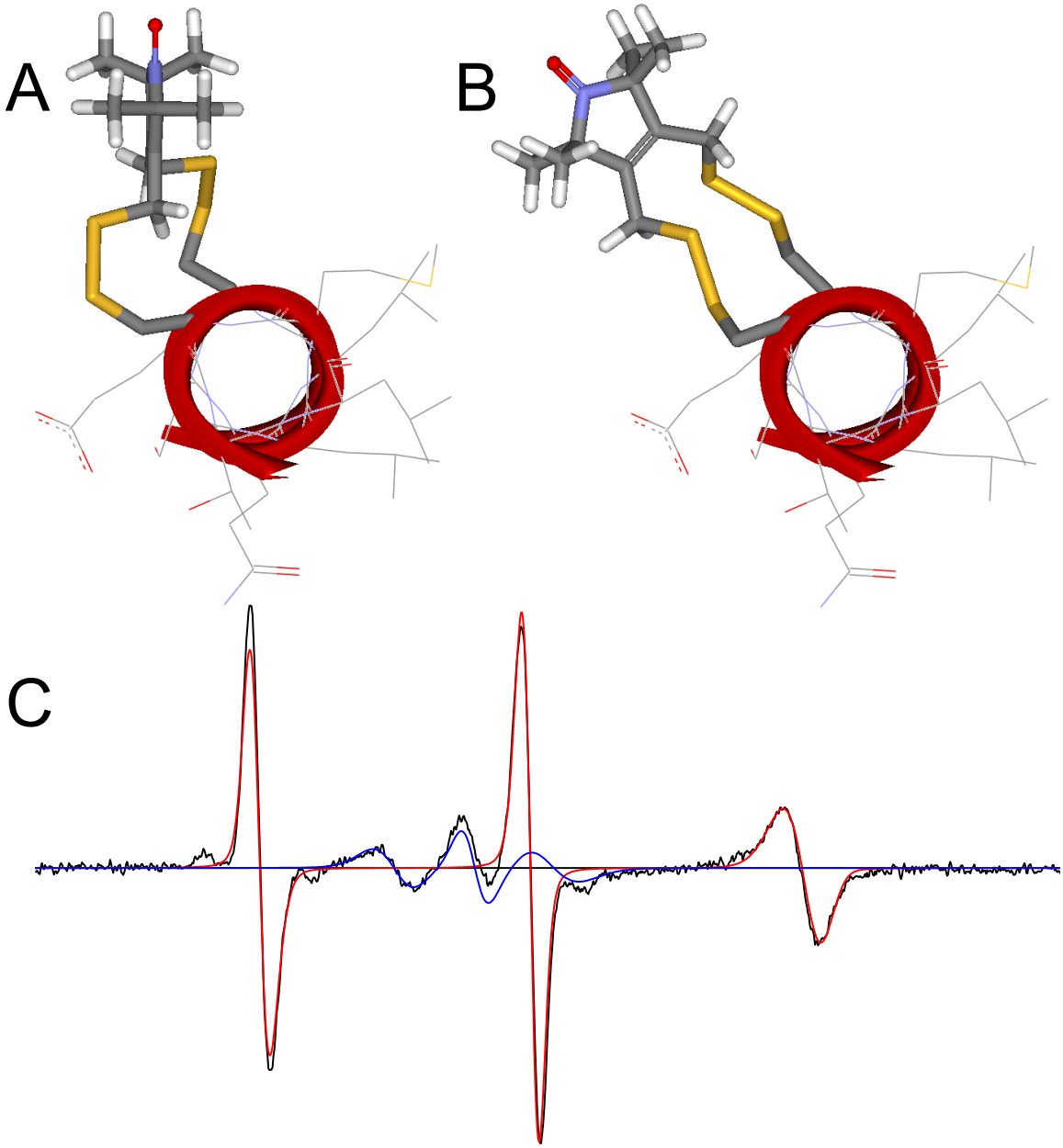

Fig. 11: uBSL conformations on a helix
The spin label principle axis is 88° (A) and 18° (B) with respect to a vector running the length of the helix core. (C) The spectrum of uBSL labeled Dicty myosin at residues A639C.A643C (black) with the components due to conformations A and B in red and blue respectively. 68% of the spectrum is due to component A.

3.4. Labeling Specificity

In a system that is being studied via site directed spin labeling, the site being labeled often is not the only cysteine present for labeling. In the case of bifunctional labeling, the presence of two cysteines allows for the potential of modification by a single spin label (crosslinking) or modification by two probes (double labeling). Interpretation of the resulting spectra requires knowledge about the specificity of labeling, such that multiple spectra features can be ascribed to a single labeling site with confidence.

3.4.1. Determining Labeling Specificity via Spin Counting

The most direct method of quantification of labeling specificity is via spin counting. The intensity of the EPR spectrum, which is the derivative of the absorption spectrum, is directly proportional to the number of spins present in the sample. By comparing the double integral of a spin labeled sample of known protein concentration to a standard sample of known spin concentration (i.e. 100 μM spin label in solution), the number of spins per protein, and thus the specificity can be obtained.

3.4.2. Quantifying the Labeling Specificity of SH1-SH2 From First Principles (published as supplementary material to (11))

Introduction

In samples with a small number of cysteines, spin counting is adequate for describing the labeling specificity. Rabbit myosin, on the other hand, has >10 cysteines present, making direct interpretation of spin counting difficult. The work presented CHAPTER 4 relies on the specific modification of SH1 and SH2. To interpret the spectral features, a more complex analysis of labeling specificity is required.

Modification of SH1 and SH2 has a quantifiable effect on the K/EDTA and Ca/K high-salt ATPases (see CHAPTER 4). While the change in ATPase activity alone can provide some insight into the specificity of spin modification of SH1 and SH2, it fails to inform about the correlation between spectrum and biochemical activity. With the added information of the number of bound spin labels per protein via spin counting, a direct measurement of spin labeling specificity is possible.

Key Assumptions

- Single S1's have discrete ATPase activities
- Individual ATPases add linearly (i.e. the proteins do not interact)
- Spin labeling SH2 can only occur in the presence of ADP and even then, SH1 reacts preferentially. Therefore, a cross-linker will always hit SH1 first and may then label SH2**.**

Proof

We begin by examining the activity of a *single* modified S1 (**Fig. 12**). An individual S1 has the following K/EDTA (K) and Ca/K (C) ATPase states corresponding to SH1 and SH2 modification:

- **Basal ATPase** (K_0, C_0), for unlabeled or non-specifically (NS) labeled S1
- **Ca Activated ATPase** (K_{min}, C_{max}), for SH1 labeled S1
- **Killed ATPase** (K_{min}, C_{min})**,** for SH1 and SH2 labeled S1

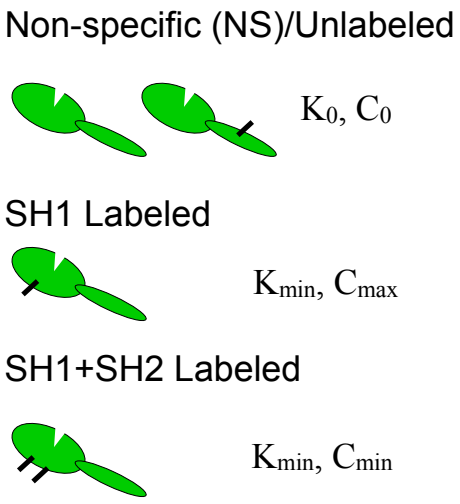

Fig. 12: Labeling Permutations
The effect of modification on the ATPases of an individual S1. Black tick marks indicate modification by a spin label.

With these definitions made, we can now perform hypothetical experiments that have a mixture of unlabeled S1 and S1 labeled either non-specifically, at SH1, or at SH1 and SH2.

We now imagine three ideal labeling experiments (Fig. 13). Here we use probes that bind exclusively to their designated site (NS, SH1, or SH1+SH2) or not at all. For each of these experiments, the bulk K and Ca ATPases for the labeled/unlabeled mixtures are merely the sum of the individual labeled and unlabeled S1 ATPases.

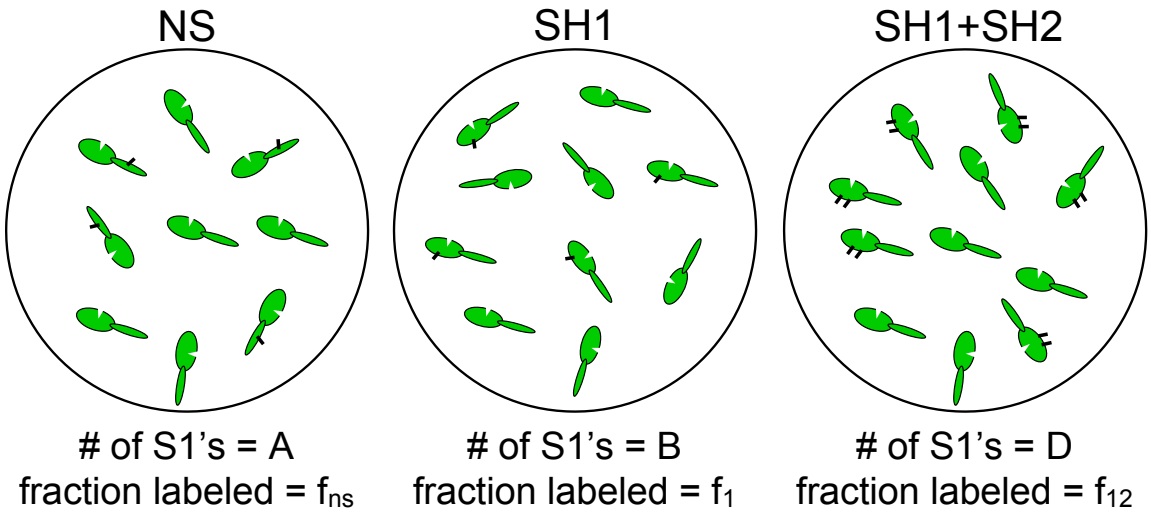

Fig. 13: Hypothetical Labeling Outcomes
Labeling thought experiments for non-specific labeling (NS), SH1 labeling and SH1+SH2 labeling. In each of these samples the number of proteins is known, as well as the fraction of those proteins labeled.

Non-specific ATPase:

$$K_{NS} = Af_{NS}K_0 + A(1-f_{NS})K_0 \qquad C_{NS} = Af_{NS}C_0 + A(1-f_{NS})C_0$$
$$= AK_0 \qquad = AC_0$$

SH1 ATPase:

$$K_1 = Bf_1K_{\min} + B(1-f_1)K_0 \qquad C_1 = Bf_1C_{\max} + B(1-f_1)C_0$$
$$= Bf_1(K_{\min} - K_0) + BK_0 \qquad = Bf_1(C_{\max} - C_0) + BC_0$$

SH1+SH2 ATPase:

$$K_{12} = Df_{12}K_{\min} + D(1-f_{12})K_0 \qquad C_{12} = Df_{12}C_{\min} + D(1-f_{12})C_0$$
$$= Df_{12}(K_{\min} - K_0) + DK_0 \qquad = Df_{12}(C_{\min} - C_0) + DC_0$$

While we have defined only three potential labeling scenarios (NS, SH1, SH1+SH2), many more combinations are possible (e.g. SH1+SH2+NS) and multiple non specific labeling sites may exist. The model proposed here is merely the simplest case without loss of generality, and the solution obtained below holds for all possible permutations of nonspecific labeling.

Now that we have determined the ATPase values for each of these imaginary experiments, we can now study the real experiment. When labeling any protein with a cysteine-specific spin label you get a mixture of specific, non-specific and unlabeled protein. In the case of crosslinking SH1-SH2 with BSL, we also have the potential of only labeling SH1 (e.g. in the absence of MgADP). Our real experiment, therefore, is analogous to the experiment we would have if we mixed our three thought experiments into a single reservoir (Fig. 14).

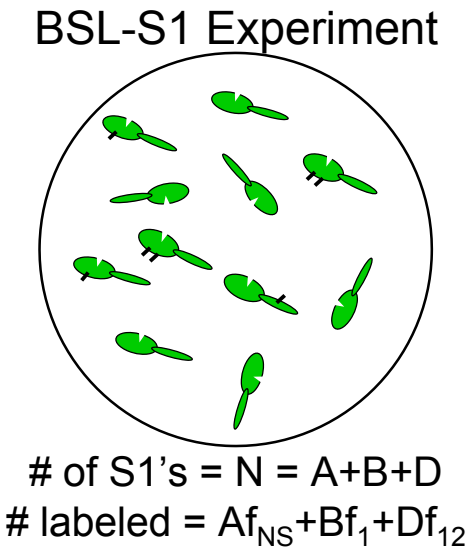

Fig. 14: BSL-S1 experiment
An actual BSL-S1 experiment, created by mixing the three hypothetical experiments.

The ATPases (K_{net}, C_{net}) for our BSL experiment are merely the sum of the ATPases for our three isolated experiments:

$$\mathbf{K_{net}} = K_{NS} + K_1 + K_{12} \qquad \mathbf{C_{net}} = C_{NS} + C_1 + C_{12}$$

and we define the spin count (X_{net}) as the number of spins per protein:

$$\mathbf{X_{net}} = \frac{Af_{NS} + Bf_1 + Df_{12}}{N} = X_{NS} + X_1 + X_{12}$$

(Note: Quantities marked in BOLD are quantities that are experimentally measured)

With the following definitions:

$\mathbf{K_0} = NK_0$ $\qquad$ $\mathbf{C_0} = NC_0$

$\mathbf{K_{min}} = NK_{min}$ $\qquad$ $\mathbf{C_{min}} = NC_{min}$

$\mathbf{C_{max}} = NC_{max}$

we obtain the following system of equations:

$$\mathbf{K_{net}} = X_1(\mathbf{K_{min}} - \mathbf{K_0}) + X_{12}(\mathbf{K_{min}} - \mathbf{K_0}) + \mathbf{K_0}$$

$$\mathbf{C_{net}} = X_1(\mathbf{C_{max}} - \mathbf{C_0}) + X_{12}(\mathbf{C_{min}} - \mathbf{C_0}) + \mathbf{C_0}$$

$$\mathbf{X_{net}} = X_{NS} + X_1 + X_{12}$$

Solving for $X_{NS,}$ X_1 and X_{12} we arrive at the final solution:

$$X_{NS} = \mathbf{X_{net}} - X_1 - X_{12}$$

$$X_1 = \frac{(\mathbf{K_{net}} - \mathbf{K_0})}{(\mathbf{K_{min}} - \mathbf{K_0})} - X_{12}$$

$$X_{12} = \frac{(\mathbf{C_{net}} - \mathbf{C_0})}{(\mathbf{C_{min}} - \mathbf{C_{max}})} - \frac{(\mathbf{K_{net}} - \mathbf{K_0})(\mathbf{C_{max}} - \mathbf{C_0})}{(\mathbf{K_{min}} - \mathbf{K_0})(\mathbf{C_{min}} - \mathbf{C_{max}})}$$

Finally, we define the specificity:

NS labeling specificity = $X_{NS}/\mathbf{X_{net}}$

SH1 specificity = $X_1/\mathbf{X_{net}}$

SH1+SH2 specificity = $X_{12}/\mathbf{X_{net}}$

Given the following values for the minimal and maximal K and Ca ATPases:

$\mathbf{K_{min}} = 0.05*\mathbf{K_0}$ (12)

$\mathbf{C_{min}} = 0.1*\mathbf{C_0}$

$\mathbf{C_{max}} = 11.4*\mathbf{C_0}$ (by extrapolation, based on $\mathbf{K_{min}}/\mathbf{K_0} = 0.05$)

we can measure the specificity for SH1+SH2 of our labeled S1 (Table 2). Thus, BSL crosslinks SH1-SH2 quite specifically under the conditions of this study.

Table 1: Labeling specificity

Sample	NS labeling	SH1 Specificity	SH1+SH2 specificity
IASL-S1	0.01	0.99	0.00
MTSSL-S1	0.04	0.88	0.08
BSL-S1	0.01	0.06	0.93

Specificity values are based upon the ATPases reported in Table 2

CHAPTER 4 - Structural Dynamics of the Actomyosin Complex Probed by a Bifunctional Spin Label That Crosslinks SH1 and SH2 (11)

Andrew R. Thompson[1†], Nariman Naber[2†], Clyde Wilson[2], Roger Cooke[2,3], and David D. Thomas[1]*

[1]Department of Biochemistry, Molecular Biology and Biophysics, University of Minnesota, Minneapolis, MN 55455
[2]Department of Biochemistry and Biophysics and [3]Cardiovascular Research Institute, University of California, San Francisco, California 94158;

Accepted to *Biophys. J.* on September 2, 2008
Reprinted with permission from Elsevier
(Rightslink license number 2160981106371)

† A.R.T. and N.N. contributed equally to this work.

*To whom correspondence should be addressed

Running title : EPR of a bifunctional spin label on myosin

Keywords: EPR, ESR, cross-linking, weak-binding, muscle fiber, pPDM

Abbreviations: BSL, Trans-3,4-bis-(methanethiosulfonylmethyl)-2,2,5,5-tetramethylpyrrolidin-1-yloxy Radical; pPDM, N,N′-(1,4-phenylene)dimaleimide; EPR, electron paramagnetic resonance; STEPR, saturation transfer electron paramagnetic resonance; IASL, 4-(2-iodoacetamido)-2,2,6,6-tetramethylpiperidine 1-oxyl; MTSSL, (1-oxy-2,2,5,5-tetramethyl-Δ^3-pyrroline-3-methyl)methanethiosulfonate.

We have used a bifunctional spin label (BSL) to crosslink Cys 707 (SH1) and Cys 697 (SH2) in the catalytic domain of myosin subfragment 1 (S1). BSL induces the same weakened ATPase activity and actin-binding affinity that is observed when SH1 and SH2 are crosslinked with pPDM, which traps an analog of the post-hydrolysis state A.M.ADP.P. EPR showed that BSL reports the global orientation and dynamics of S1. When bound to actin in oriented muscle fibers in the absence of ATP, BSL-S1 showed almost complete orientational disorder, as reported previously for the weakly bound A.M.ATP. In contrast, helical order is observed for the strongly bound state A.M. Saturation transfer EPR showed that the disorder of crosslinked S1 on actin is nearly static on the microsecond time scale, at least 30 times slower than that of A.M.ATP. We conclude that crosslinked S1 exhibits rotational disorder comparable to that of A.M.ATP, slow rotational mobility comparable to that of A.M, and intermediate actin affinity. These results support the hypothesis that the catalytic domain of myosin is orientationally disordered on actin in a post-hydrolysis state in the early stages of force generation.

4.1. Introduction

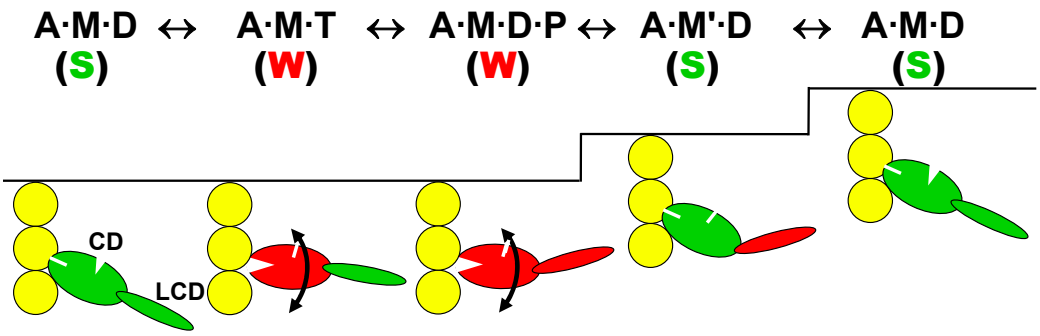

Fig. 15: Canonical Power Stroke
Structural model by which ATP hydrolysis is coupled to movement of actin (yellow) by myosin's catalytic domain (CD) and light-chain domain (LCD). Red and green colors signify pre-and post-force generating conformations, arrows signify orientational disorder, and steps indicate stages in the cycles where force and movement are likely to be imparted to actin. A = actin, M = myosin, T = ATP, D = ADP, P = inorganic phosphate. S = strong-binding (force-generating) structural state, W = weak-binding structural state. Prime symbol (′) indicates a second structural state corresponding to the same biochemical state (defined by the active-site ligand).

Muscle contraction is produced when actin activates the hydrolysis of ATP by myosin, resulting in relative translation of the two proteins. Force generation has been proposed to originate from transition of the myosin catalytic domain from a disordered state of weak actin binding to an ordered state of strong actin binding, followed by a lever arm rotation of the light chain domain (13-15) (Fig. 15). The strongly bound complexes A.M and A.M.D have been studied in great detail: In the absence of nucleotide or in the presence of MgADP, actin and myosin interact such that the orientations of both the catalytic (16,17) and light-chain (7) domains are well defined with respect to the actin filament axis. However, much less is known about the structures of the weakly bound complexes (A.M.T and A.M.D.P), not only because of their dynamic disorder, but also because they are short-lived. Saturation transfer EPR (STEPR) in the steady state of ATP hydrolysis (18,19), or in the presence of ATPγS (20,21) has shown clearly that weakly attached

myosin heads undergo large-amplitude rotational motions with correlation times in the range of 1 to 20 μs, and this is consistent with the orientationally disordered appearance of S1 bound to actin in electron micrographs of similar weakly bound complexes (22-24).

However, all of these EPR and EM experiments were done under conditions in which the predominant actin-attached states were most likely the prehydrolysis complex A.M.T. The post-hydrolysis complex A.M.D.P is potentially of much more interest, since there is evidence that force generation begins in this biochemical state, before phosphate is released (25,26). This complex has remained elusive for two reasons: (a) Actin greatly accelerates the release of P_i from myosin (converting A.M.D.P to A.M.D); and (b) actin shifts the equilibrium constant for hydrolysis toward the prehydrolysis state (converting A.M.D.P to A.M.T) by a factor of 20 (27). It has not proven feasible to prepare a stable complex of actin with myosin using the post-hydrolysis analogs ADP.V_i and ADP.AlF_4, because actin rapidly dissociates the phosphate analogs from the complex (28,29). The nucleotide analogs AMPPNP and pyrophosphate do remain bound in ternary complexes with actin and myosin, but these complexes are indistinguishable from the strongly bound complex A.M.D (20,30,31).

There is one relatively stable equilibrium complex, though, that has been proposed to have the biochemical and structural properties of the ternary complex A.M.D.P: the complex of actin with myosin S1 that has been reacted with pPDM, which specifically crosslinks SH1 (Cys 707) to SH2 (Cys 697) (32-34). It was found that pPDM-S1 exhibits weak actin binding, with an actin affinity at low ionic strength (K_d = 30 μM) only about 3 times stronger than S1.ATP, 100 times weaker than S1.AMPPNP, and 1000 times weaker than S1.ADP (33). The observation that ADP-bound S1 has three

orders of magnitude greater actin affinity seems surprising, considering that pPDM traps MgADP during crosslinking and MgADP accelerates the reaction of pPDM with S1 (35,36). However, the removal of MgADP after pPDM crosslinking has little effect on the properties of pPDM-S1, so the weak binding is not a function of the trapped nucleotide (32). Chemical (36), spectroscopic (37), and crystallographic (6) analysis suggested a structural explanation: pPDM is much too short to crosslink Cys697 to Cys707 in the crystal structure of S1 (2), so nucleotide binding results in the disordering of the intervening SH1 helix, permitting the two Cys residues to approach, at least transiently, within the pPDM crosslinking distance. Thus it is likely that pPDM-S1 is a structural and functional analog for a weak-binding post-hydrolysis state A.M.D.P, so there is a need for spectroscopic data to characterize the structure and dynamics of this complex.

However, the reaction of pPDM blocks SH1 and SH2, thus preventing use of the SH1-bound spin labels that have been so useful in characterizing the orientation and dynamics of myosin catalytic domains bound to actin. To solve this problem, in the present study we use a bifunctional spin label (BSL) that is itself a cysteine cross-linker. We show that it binds rigidly and specifically to S1, crosslinking SH1 and SH2. To obtain information about the orientation of the spin-labeled S1 relative to actin, and to overcome the weak binding of the crosslinked S1 to actin, we perform EPR experiments in skinned muscle fibers, where the free actin concentration is ~360μM (38). We decorate these fibers with spin-labeled S1 and then use both conventional and STEPR to determine the orientation and rotational dynamics of the actin-attached myosin heads in this weak-binding analog of A.M.D.P.

4.2. Methods

Preparation of Proteins and Muscle Fibers

Myosin, chymotryptic myosin subfragment 1 (S1), and actin were prepared from rabbit skeletal muscle as described previously (28). Concentrations were determined from UV absorbance: [myosin] = $(A_{280}-A_{320})/(2.49 \times 10^5\ M^{-1}cm^{-1})$, [S1] = $(A_{280}-A_{320})/(8.07 \times 10^4\ M^{-1}cm^{-1})$, [actin] = $(A_{290}-A_{320})/(2.71 \times 10^4\ M^{-1}cm^{-1})$. Glycerinated rabbit psoas muscle fiber strips (approximately 2 mm diameter) were prepared and stored in a 1:1 (vol:vol) mixture of rigor buffer (120 mM KCl, 25 mM MOPS, 2 mM $MgCl_2$, 1 mM EGTA, pH 7.0) and glycerol at -20^{o}C for up to 6 months without significant loss of function (39). All preparations and experiments below were carried out at 4^{o}C.

Monofunctional Labeling

SH1 (Cys 707) of the myosin S1 head was spin-labeled with the monofunctional probes IASL (Sigma–Aldrich, St. Louis, MO) or MTSSL (Toronto Research Chemicals, North York, ON) as follows: 20 μM S1 was incubated with 30 μM spin label at 4^{o}C in monofunctional labeling buffer (50 mM MOPS, 50 mM KCl, pH 7.0) for 16 h for IASL or 2 h for MTSSL. The unbound spin label was removed by passing the labeled protein twice through a Pierce Zeba size-exclusion spin column (Thermo Fisher Scientific Inc., Rockford, IL), which was equilibrated with monofunctional labeling buffer. S1 was then concentrated and transferred to low salt buffer (LSB, 2 mM $MgCl_2$, 1 mM EGTA, 40 mM MOPS pH 7) using an Amicon Centricon membrane concentrator (Millipore, Billerica, MA). The resulting purified protein is termed IASL-S1 or MTSSL-S1. To prepare IASL-myosin, the same procedure was used, except that removal of unbound label and

concentration were accomplished by sedimentation and resuspension of myosin filaments (40).

Bifunctional Labeling

SH1 (Cys 707) and SH2 (Cys 697) were crosslinked using either BSL (Toronto Research Chemicals, North York, ON) or pPDM (Sigma–Aldrich, St. Louis, MO). To a solution of 20 μM S1 in crosslinking buffer (1 mM ADP, 2mM $MgCl_2$, 100 mM KCl, 40 mM Tris, pH 7.8), 24 μM BSL or 30 μM pPDM was added from freshly prepared stock solutions in DMF, such that the final DMF concentration never exceeded 1%. After 1 h, the unreacted crosslinker was removed and the protein was concentrated as described above for monofunctional labeling. The unreacted and monofunctionally labeled S1 were removed by co-sedimentation with actin in LSB. The resulting purified preparations are termed BSL-S1 and pPDM-S1 respectively. To prepare BSL-myosin, the same procedure was used, except that removal of unbound label was accomplished by sedimentation and resuspension of myosin filaments (40).

Biochemical Assays

To assess Cys labeling of SH1 and SH2, the K/EDTA and Ca/K ATPase activities were measured at high ionic strength by measuring phosphate liberation after acid quench (41). The incubation buffer (25°C) contained 50 mM MOPS and 0.6M KCl, pH 7.5, and either 5 mM EDTA (K/EDTA ATPase) or 10 mM $CaCl_2$ (Ca/K ATPase). The activity was checked by ATPase assays both before and after the acquisition of spectra to ensure stability of the observed state. The equilibrium constant for dissociation of labeled S1 from actin (K_d) was measured in LSB by cosedimentation (42).

To assess the weak or strong mode by which S1 binds to actin, the quenching of pyrene-labeled actin was measured (43). Actin was labeled at Cys 374 with pyrene iodoacetamide (Invitrogen, Carlsbad, CA) (28), and fluorescence was measured using a Varian Cary Eclipse fluorometer (Varian Inc., Palo Alto, CA), with excitation and emission at 350 nm and 409 nm, respectively. S1 or labeled S1 was then added in excess of actin. Strong binding of S1 to actin was noted by a quenching of pyrene fluorescence, whereas weak binding (e.g., in the presence of saturating ATP) produced no change from the basal pyrene fluorescence (43).

EPR Spectroscopy

For EPR experiments on spin-labeled myosin or S1 in solution, samples were dialyzed into LSB, adjusted to a final concentration of 100 μM myosin heads, and were placed into a flame-sealed glass capillary (50 μL Wiretrol, Drummond Scientific, Broomall, PA). For experiments on actin-bound S1, skinned muscle fiber strips were dissected into bundles of approximately 0.5 mm diameter. The fibers were then soaked in the spin-labeled S1 solution in LSB (either IASL-S1 or BSL-S1), at a concentration of 100 μM or higher. After at least 2 h the fibers were washed several times with LSB to remove any unbound S1.

S1-decorated muscle fiber bundles were cut into 0.5 cm lengths and aligned to be perpendicular to the long axis of a quartz tissue flat cell that contained a well of dimensions 0.5 x 1.0 x 0.05 cm (WG-806-Q, Wilmad-Labglass, Buena, NJ). Excess moisture was wicked away from the fibers with a Kimwipe (Kimberly-Clark, Neenah, WI) and a cover-slip was placed over the sample well, sealed with vacuum grease to

prevent sample dehydration. The flat cell assembly was then centered in the EPR cavity using Teflon collets and the fiber axis was manually oriented parallel or perpendicular to the external magnetic field. To obtain randomly oriented fibers for STEPR and other experiments, fibers were minced with a razor blade, and random orientation was verified by showing that the spectrum was insensitive to the flat cell's orientation in the magnetic field. STEPR experiments were performed with the flat cell plane perpendicular to the applied field.

EPR spectra were obtained at X-band (9.5 GHz) with either a Bruker (Billerica, MA) EMX or E500 spectrometer, using a TE102 (Bruker 4102ST) cavity. The sample temperature was maintained at 4°C by flowing cold N_2 gas through a nozzle attached to the optical port on the front of the cavity. The sweep width was 120 G (1024 points), sweep time was typically 40s, and the center field value B_C was set proportionally to the microwave frequency ($B_C = \nu/2.803$ MHz/G, corresponding to a g value of 2.0027, the value of g_z for a typical nitroxide) so that all spectra were equivalently aligned.

Conventional (V_1) spectra were recorded at a microwave field amplitude of B_1 = 0.14 G, with modulation frequency ν_m = 100 kHz (first harmonic), peak-to-peak modulation amplitude B_m = 1 G, modulation phase ϕ_m = 0 degrees (maximum signal), and filter time constant τ_F = conversion time. STEPR (V_2') spectra were recorded essentially as described previously (44), with B_1 = 0.25 G, ν_m = 50 kHz, B_m = 5 G, phase-sensitive detection at 100 kHz (second harmonic), ϕ_m = 90 degrees (minimum signal at non-saturating power), and τ_F = twice the conversion time (Due to the higher B_m, this does not distort the spectrum, since the linewidths are greater.). Typically, the

signal/noise per scan was lower for V_2' than for V_1, so the number of scans was increased; typical acquisition times were 5 min for V_1 and 30 min for V_2'.

For each different sample configuration, B_1 was determined from $B_1 = C P^{1/2} Q_0/Q$, where C was determined by calibration with a sample of known saturation properties (peroxylamine disulfonate (44)), Q_0 is the cavity quality factor (measured by the spectrometer) during the original calibration, and Q is the value measured for each experiment. P was adjusted to obtain the desired B_1 value. For the standard flat cell configuration, C = 1.0 $G/W^{1/2}$ and Q_0 = 1200, so P was set at 20 mW x Q/1200 for V_1 and 63 mW x Q/1200 for V_2'.

Conventional EPR spectra (V_1) of spin-labeled S1 attached to actin in oriented muscle fibers were analyzed to determine the orientational distribution of the nitroxide spin label relative to the muscle fiber axis, using computational simulation and least-squares minimization, as described previously (16,45). Briefly, the spectrum of minced fibers or precipitated S1 was first fit to obtain the orientation-independent parameters, such as the effective values for the anisotropic T and g matrices, and the linewidths. Using these values, spectra of oriented fibers were then fit to the orientational distribution of the spin label relative to the fiber axis, as defined by the center (θ_0') and width ($\Delta\theta'$, full width at half maximum) of the presumed Gaussian orientational distribution.

STEPR spectra (V_2') of randomly oriented samples (in solution or minced fibers) were analyzed to determine the effective rotational correlation time τ_R, by measuring the ratio of the features L" and L for μs-ms motion or C' and C for sub-μs motion, as defined previously (44). The position of L" was taken as an average of height above baseline of the data 5-10G to the right of L. The measured ratios L"/L and C'/C were then used to

determine the rotational correlation time by comparison to the data for a model system shown in Figure 3 of (44).

Quantification of the extent of spin labeling (spin labels bound per S1) was done by digital analysis of EPR spectra (46). Briefly, the double integral of the V_1 spectrum of a known concentration of S1 (typically 100 μM) was obtained at sufficiently low power to avoid saturation (typically 1 mW). This value was then compared to the double integral of a sample of known spin label concentration at the same microwave power and B_1 value, to obtain the number of spin labels per S1.

4.3. Results

BSL Crosslinks SH1 and SH2.

The K-ATPase and Ca-ATPase activities, in conjunction with spin counts, were used to assess the extent and specificity of SH1 and SH2 labeling (Table 2). In both cases of monofunctional labeling (with IASL and MTSSL), the K-ATPase is inhibited by >85% and Ca-ATPase activated by >90%, indicating an essentially complete reaction with SH1 but not SH2 (47). For both BSL-S1 and pPDM-S1, the K-ATPase is also strongly inhibited, indicating essentially complete reaction with SH1, but the Ca-ATPase is less than 10% of that observed for IASL-S1 and MTSSL-S1, implying that at least 90% of SH2 has also been labeled (48). The result of EPR-based quantitation of the spin label concentration (METHODS) yields 0.94 ± 0.07 moles of BSL per mole of S1. We conclude that virtually every S1 has both SH1 and SH2 blocked by a single spin label, which must be crosslinking the two cysteines (see Supplementary Material). Cosedimentation with actin showed that monofunctionally labeled S1 binds actin strongly (K_d < 1 μM), in agreement with previous results (20), while both crosslinked S1 species bind actin much more weakly (K_d ≈ 30 μM) (Table 2). Similarly, monofunctionally labeled S1 strongly quenched the fluorescence of pyrene-labeled actin, while neither BSL-S1 nor pPDM-S1 caused significant quenching, even when added at concentrations comparable to K_d. These results confirm that monofunctionally labeled S1 binds strongly to actin, while BSL-S1 binds weakly and has the same effect on actin structure as pPDM-S1 or S1.ATP (43). We conclude that BSL completely and specifically crosslinks SH1 and SH2, giving BSL-S1 the same weak actin-binding properties as pPDM-S1.

The conventional (V_1) EPR spectra of both IASL-S1 and BSL-S1 indicate that the nitroxide probes are strongly immobilized on the protein, with an outer splitting $2T_{||}$' = 69.5 G (Fig. 16) corresponding to that predicted for slow tumbling of S1 in solution, with a rotational correlation time of about 200 ns (49). In contrast MTSSL, the monofunctional version of BSL, shows a narrow spectrum indicating a high degree of mobility in the subnanosecond time range (Fig. 16), despite its attachment to the same SH1 site as IASL. This result indicates that BSL's immobilization is due to bifunctional attachment to S1, at both SH1 and SH2, as indicated by Table 2.

Table 2: The effect of labeling S1 on ATPase activity and actin binding

Sample	Relative K-ATPase	Relative Ca-ATPase	K_d
IASL-S1	11 ± 4	1080 ± 70	< 1 μM
MTSSL-S1	13 ± 7	960 ± 90	< 1 μM
BSL-S1	8 ± 6	79 ± 6	31 ± 6 μM
pPDM-S1	12 ± 9	45 ± 7	30 ± 7 μM

ATPase values are % (mean ± SE) of unmodified S1 values, 8.7 ± 0.5 s^{-1} (K-ATPase) and 0.92 ± 0.07 s^{-1} (Ca-ATPase).

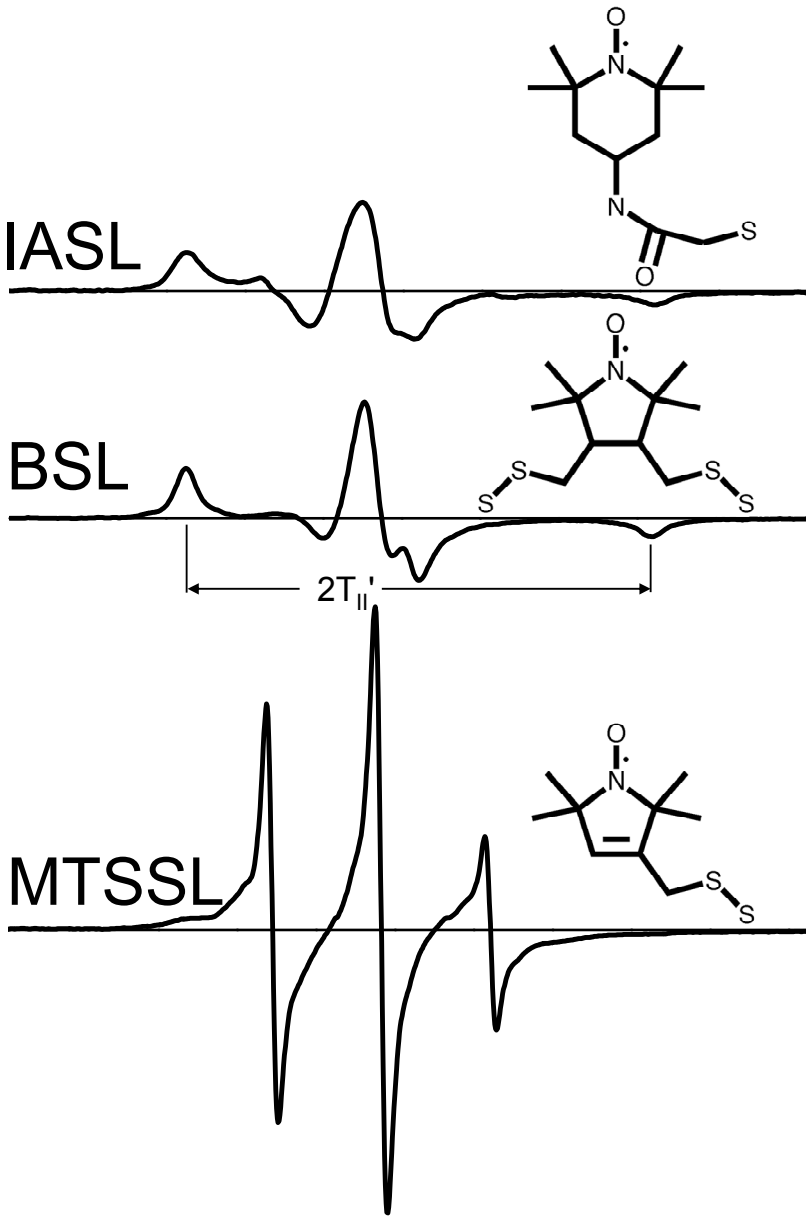

Fig. 16: Spin labeled S1
Conventional (V_1) EPR spectra of spin-labeled S1 (100 μM) in LSB at 4°C.

EPR of Oriented Muscle Fibers Decorated With S1

EPR has a high degree of sensitivity to the orientational distribution of a spin label with respect to the externally applied magnetic field. The spectrum is sensitive primarily to the angle θ between the spin label's principal axis and the field. In a well oriented system, such as skinned muscle fibers, this sensitivity can be used to measure the orientation of the probe with respect to the fiber axis (θ') (16), as simulated in Fig. 17. When the fibers are aligned on a flat cell, the fiber axis can be oriented either parallel (red, where θ = θ′) or perpendicular (blue, where θ′ exhibits more disorder due to helical symmetry, as illustrated in Fig. 17) to the applied magnetic field.

The orientation of spin-labeled S1 bound to actin, with respect to the actin filament axis, was determined from EPR spectra of S1-decorated muscle fibers (Fig. 18). As shown previously, fibers decorated with IASL-S1 show a high degree of orientational

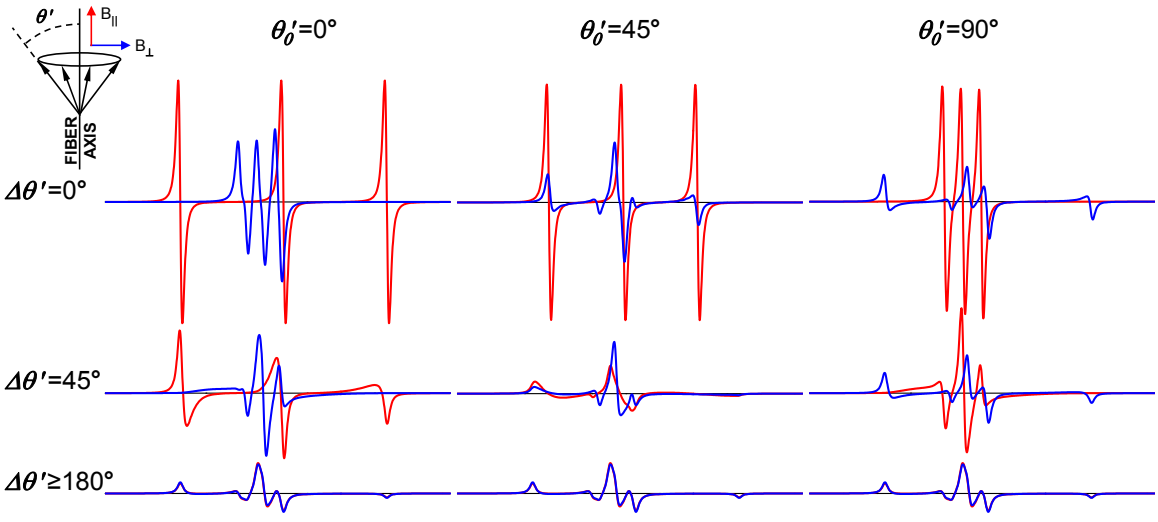

Fig. 17: The orientational sensitivity of EPR
Simulated EPR spectra, showing the dependence of conventional (V_1) EPR spectra on the orientation θ′ of the nitroxide spin label's principal axis relative to the muscle fiber (actin filament) axis. A Gaussian distribution of θ′is assumed, where θ_0' is the center of the distribution and Δθ′ is the full width at half maximum. Spectra are shown corresponding to the muscle fiber axis both parallel (red) and perpendicular (blue) to the applied magnetic field (B).

order with respect to the fiber axis (Fig. 18, top), indicating that the angles (defined in Fig. 17) are $\theta' = 68 \pm 1^{o}$ and $\Delta\theta' = 17 \pm 2^{o}$ (16). In contrast, fibers decorated with BSL-S1 yield spectra that are characteristic of near random orientation ($\Delta\theta' \geq 90°$), having little sensitivity to sample orientation with respect to the applied magnetic field (Fig. 18, *bottom*). We conclude that BSL-S1, bound to oriented actin in the muscle fiber, shows a profound degree of orientational disorder relative to the actin filament axis. The next question: is this disorder dynamic on the microsecond time scale, as observed previously for S1 weakly bound to actin in a ternary complex with ATP (18), or static? This question can only be answered by STEPR.

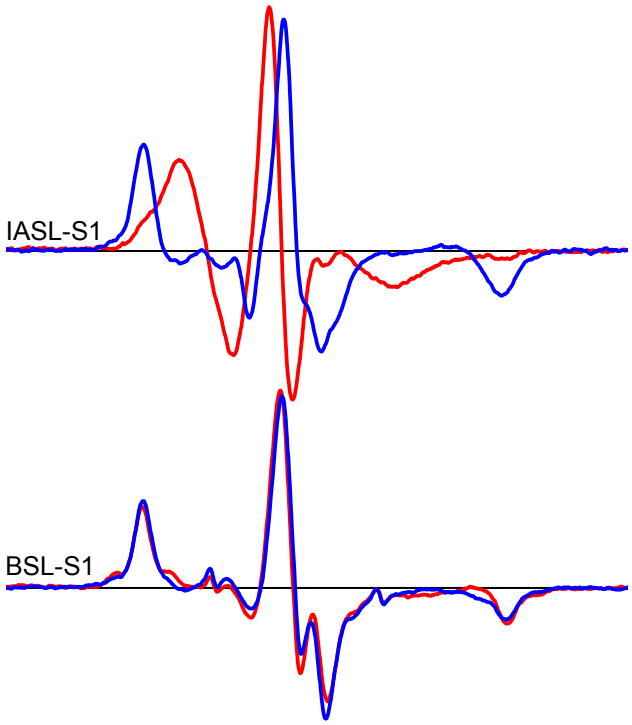

Fig. 18: SH1 modification vs. SH1-SH2 crosslinking
Oriented muscle fibers decorated with spin-labeled S1. The spectra were recorded with the fiber axis aligned parallel (red) or perpendicular (blue) to the external magnetic field in a quartz flat cell.

STEPR

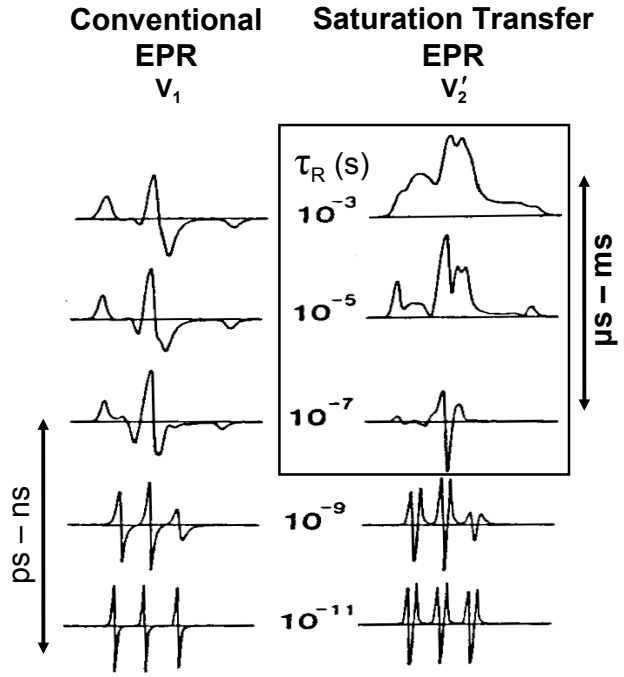

Fig. 19: Dynamics and EPR
Dependence of conventional (V_1, left) and saturation transfer (V_2', right) EPR spectra on isotropic rotational correlation time (50).

In addition to orientation, EPR is also sensitive to rotational dynamics from the ps to ms time scales. To ensure that any observed spectral changes are due only to dynamics, samples must be randomly oriented. However, conventional (V_1) EPR is sensitive only to motions with rotational correlation times (τ_R) in the ps to ns range (Fig. 19, *left*). For slower motions (μs to ms), such as those likely to occur for a large protein or within a large protein assembly, STEPR must be used (Fig. 19, *right*) (44,51).

Conventional EPR (V_1) and STEPR (V_2') measurements were performed on randomly oriented samples of IASL-S1 and BSL-S1 (Fig. 20) in a variety of environments, in order to determine the dynamics of the actin bound catalytic domain. The conventional (V_1) spectra for both IASL-S1 and BSL-S1 have virtually no sensitivity to the different protein environments (Fig. 20), and all spectra have the characteristic "powder" shape, indicating that the rotational correlation time is greater than 0.1 μs (Fig. 19). In contrast, STEPR (V_2') is quite sensitive to the changes in S1 environment (Fig. 20), demonstrating dynamics in the μs-to-ms time range (Fig. 19). Rotational correlation times for V_2' spectra were determined from lineheight ratio parameters as described in METHODS (44) (Table 3). We found that the rotational correlation times for BSL-S1 and IASL-S1 are identical within experimental error in all of the preparations studied (Table 3). The noticeable difference in V_2' lineshape between the two samples is due to

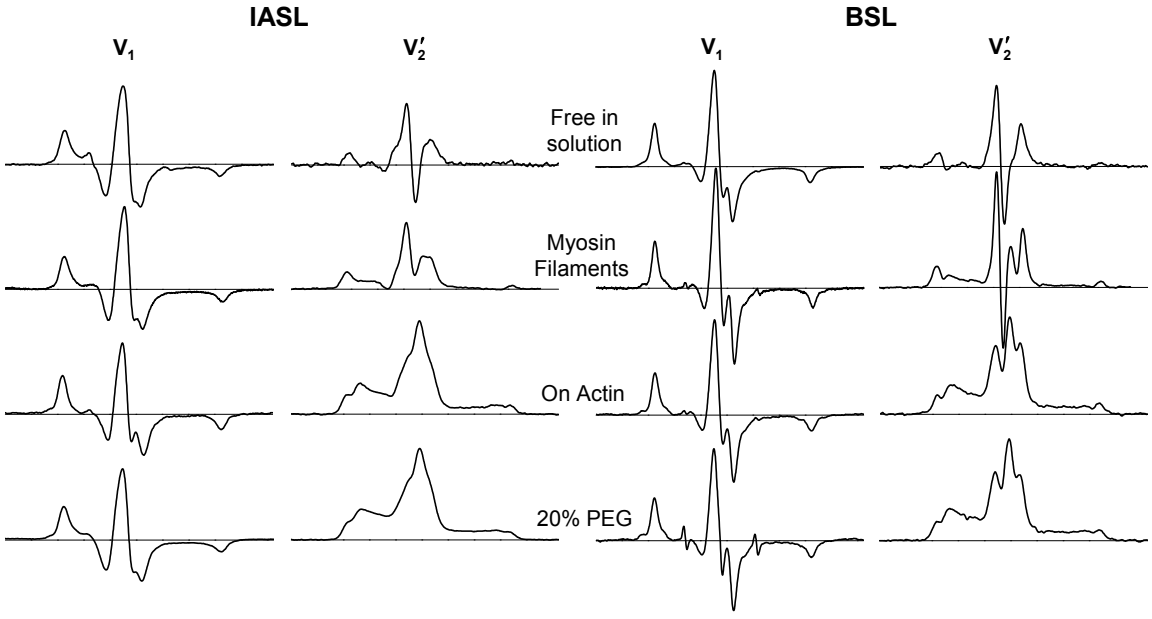

Fig. 20: STEPR of spin labeled S1
Conventional (V_1) and saturation transfer (V_2') EPR spectra for IASL-S1 (left) and BSL-S1 (right).

the narrower intrinsic linewidth observed for BSL-S1, probably due to the more rigid coupling of the probe to the protein, which appears to affect small amplitude motions that have little effect on the V2′ lineshape parameters (52). For both spin labels, S1 free in solution (Fig. 20, *top row*) gave spectra characteristic of sub-μs rotational motion (Table 3), as expected for the rigid-body tumbling of S1, while S1 precipitated in 20% polyethylene glycol (Fig. 20, *bottom row*) gave spectra approaching the rigid limit for STEPR, implying correlation times ≥ 1 ms (Table 3). Therefore, the μs rotational correlation times measured for other samples reflect accurately the global dynamics of the myosin head. Most importantly, the rotational correlation times for both IASL-S1 and BSL-S1 bound to actin (Fig. 20, *third row*) are both approximately 600 μs, nearly at the static limit for STEPR. This similarity in rotational correlation time is remarkable, in light of the dramatic difference in the orientational distributions for these two spin labels (Fig. 18). The extremely slow motion is not surprising for IASL-S1, since this protein binds quite strongly to actin (K_d < 1 μM, Table 2). However, BSL-S1 binds much more weakly (K_d = 30 μM, Table 2) and has the same slow motion, despite previous reports that weak-binding myosin heads rotate on actin at least 30 times faster (18,53,54). This fast motion of weakly bound heads is simulated here for our probes by myosin filaments, which have a correlation time of 20 μs (Table 3), approximately the same as observed previously for S1 weakly bound to actin in a ternary complex with ATP (18,54). Thus BSL-S1 has the same orientational disorder on actin as observed for ATP-induced weak binding, but rotates 30 times more slowly.

Table 3: Effective rotational correlation times (τ_R) from V_2' spectra (Fig. 20)

Sample	L''/L	C'/C	τ_R (μs)
IASL-S1		-0.26±0.01	≤ 0.50
IASL-myosin	0.47±0.01		18 ± 1
MSL-S1 on actin + ATPγS(20)	0.54±0.05		24 ± 5
IASL-S1 on actin	1.44±0.02		560 ± 40
IASL-S1 in 20% PEG	1.58±0.02		≥ 1000
BSL-S1		0.18±0.01	≤ 0.50
BSL-myosin	0.51±0.01		21 ± 1
BSL-S1 on actin	1.46±0.01		600 ± 20
BSL-S1 in 20% PEG	1.60±0.01		≥ 1000

Values are mean ± SE (n = 3-6).

4.4. Discussion

Summary of Results

When myosin S1 is reacted with a stoichiometric amount of BSL in the presence of ADP, a stable ternary complex is formed between the label, SH1 and SH2. Hi-salt ATPase activities (Table 2) and the EPR spectral intensity reveal that this reaction is highly specific and complete. Binding assays reveal that the affinity for actin (Table 2) is similar to that of the well studied pPDM-S1 complex: BSL-S1 (K_d = 30 μM) binds much more weakly than S1 (K_d < 1 μM) but 3 times more strongly than S1.ATP (K_d = 100 μM at the same ionic strength (33)). The failure to quench pyrene-labeled actin fluorescence, even at concentrations exceeding K_d, confirms that the structural interactions in the acto-S1 complex are of the same weak-binding nature as observed for pPDM. Consistent with the observed weak binding, EPR of BSL-S1 bound to actin reveals virtually complete orientational disorder relative to actin (Fig. 18), as observed previously for S1 in ternary complexes with actin and ATP (discussed below). This is in sharp contrast to the high degree of orientational order observed for the strongly bound IASL-S1. STEPR of these two preparations, on the other hand, reveals similar sub-millisecond rotational dynamics (Fig. 20), 30 times slower than observed for the ternary complex A.M.T, as modeled by A.M.ATPγS (Table 3)(20).

Interpretation of Results

During the actomyosin ATPase cycle, myosin undergoes a weak-to-strong binding transition, accompanied by ATP hydrolysis and P_i release, in which the catalytic domain undergoes a disorder-to-order transition at the actin interface and the light chain domain rotates as a lever arm (Fig. 15). This two-step structural transition is proposed to generate force in muscle contraction (13-15). The weak-binding state, simulated here by myosin filaments (Fig. 20, *second row*), exhibits a high degree of orientational disorder on the microsecond time scale, similar to that of the A.M.T state measured directly (20,53). The strong-binding state, represented by IASL-S1, makes a bond to actin with a high degree of orientational order (Fig. 18, *top*) and at least 30-fold slower motion than A.M.T (Table 3). BSL-S1 exhibits characteristics of each: Its motion is as slow (τ_R = 600 μs) as in the strong-binding state (τ_R = 560 μs, Table 3), but its orientation on actin is as poorly defined as in the weak-binding state (Fig. 18). These properties are accompanied by an affinity for actin that is also intermediate between the weak-binding and strong-binding states, as in the case of pPDM-S1 (Table 2). What biochemical intermediate might be trapped by the BSL crosslinker? To increase the specificity of BSL for SH1 and SH2 crosslinking, the reaction was done in the presence of MgADP, stoichiometrically trapping the nucleotide upon crosslinking. It would be natural, then, to conclude that we have trapped a state toward the end of the power stroke. This conclusion is greatly weakened, though, by the observations that the S1.ADP state binds actin 1000 times more strongly than does crosslinked S1 (33) and that removal of the bound ADP only slightly affects actin affinity (32). Therefore, we conclude that the SH1-SH2 helix is always in

equilibrium between crosslinkable (disordered) and uncrosslinkable (ordered) conformational states, and the nucleotide simply shifts the equilibrium between these two states, and thus the rate of crosslinking. Indeed, it has been shown that oPDM (*N*,*N*'-1,2-phenylene dimaleimide), a crosslinker of similar dimensions to BSL, reacts with SH1-SH2 at least 4 times faster in the presence of a post-hydrolysis analog (ADP vanadate or ADP aluminum fluoride) than a pre-hydrolysis analog (55). This suggests that BSL crosslinking traps S1 in a state that mimics a post-hydrolysis ternary complex, A.M.ADP.P_i. This represents an important breakthrough, since this complex is proposed to initiate force generation (25,26) but is virtually impossible to trap in solution in the absence of crosslinking, as discussed in the Introduction.

Relationship to Previous Results

Our observation of slow orientational disorder of crosslinked S1 is consistent with previous studies. Electron microscopy of pPDM-S1 bound to actin via a zero-length crosslinker reveals a high degree of orientational disorder (56), in stark contrast to the highly ordered arrowhead-shaped rigor acto-S1 complex (57). This level of orientational disorder is quite similar to that observed by EM when S1 is bound to actin in the presence of saturating ATP (22-24), and to the dynamic orientational disorder observed by EPR for actin-bound S1 in the presence of ATP (18,53) or ATPγS ((20), Table 2). Even in intact muscle fibers, myosin heads bound to actin and ATP, in the absence of calcium, show similar dynamic disorder of the catalytic domain (58). However, EPR of spin labeled muscle fibers in the presence of aluminum fluoride and calcium revealed a state similar to that observed in the present study for BSL-S1 – slow disorder of the catalytic domain,

leading the authors to suggest that this represents an intermediate state between weak binding and force generation (59). Together, these results suggest that the myosin catalytic domain enters the powerstroke when its dynamic (microsecond) disorder becomes much slower.

Alternative Explanations

It is conceivable that the observed orientational disorder of BSL-S1 is due to internal disorder within S1, rather than global disorder of S1 due to weakening of the actomyosin interface. However, even if the SH1-SH2 helix unfolds, it seems unlikely that the orientational disorder would be as complete as we observe ($\Delta\theta' \geq 90^{o}$, Fig. 17, Fig. 18) while also being so slow. Note that the STEPR spectra are not consistent with more rapid (i.e., submicrosecond) motions that are more restricted, since STEPR measures the correlation time directly and accurately in the time domain from 0.1 to 1 ms (52). Furthermore, it is difficult to discount the orientational disorder observed in EM, as discussed above. Finally, it is not possible that the disorder is due to a significant population of dissociated heads, since the dissociation constant (30 μM, Table 2) is ~10 times less than the concentration of unoccupied actin (38).

Relationship to the Mechanism of Force Generation

Our biochemical and EPR data indicate that we have trapped an intermediate state of the catalytic domain along the pathway from weak-binding disorder (**W**) to strong-binding order (**S**). In this new state, shown as A.M′.D.P (**WS**) in the revised scheme (Fig. 21), the myosin catalytic domain shares the orientational disorder of weak binding (red)

and the slow dynamics of strong binding (green). The nucleotide-binding cleft is also beginning to open, as evidenced by the ability to freely exchange the trapped nucleotide with other nucleotides when on actin (32), providing the impetus for product release and the generation of mechanical force. We propose that the relatively slow rotational dynamics of this state, compared with the truly weak-binding states A.M.T and A.M.D.P, confers enough mechanical stability at the actomyosin interface to begin generating (and bearing) force. This model is consistent with mechanical evidence, both in muscle fibers and in isolated actomyosin, that the A.M′.D.P state initiates force generation (25,26).

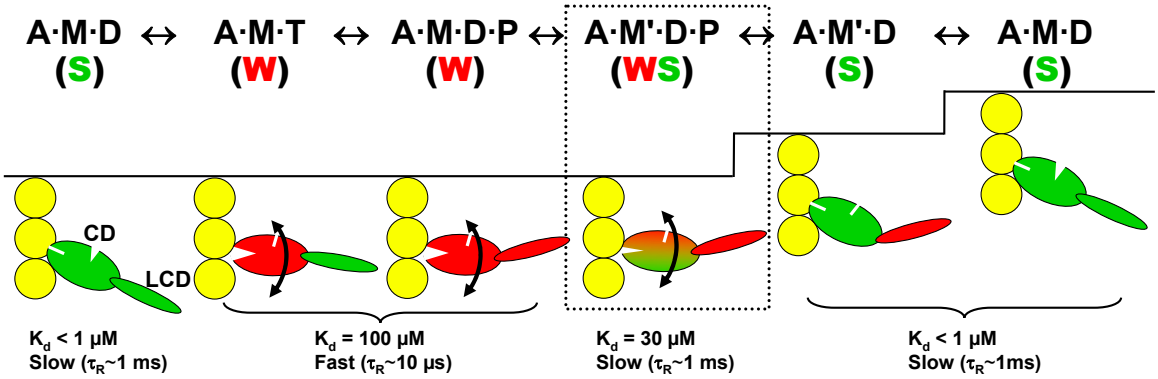

Fig. 21: Canonical model with the trapped weak binding state
A revised model for the coupling of actomyosin ATP hydrolysis to force and movement, focusing on the coupling of biochemical transitions to structural dynamics of the myosin catalytic domain (CD). The structural states and definitions are the same as in Fig. 15, except for the WS intermediate defined by the present study. Text under each state indicates distinguishing properties of the catalytic domain. Prime symbol (′) indicates a second structural state corresponding to the same biochemical state (defined by the active-site ligand). Although this scheme shows that structural transitions in the catalytic domain are completed before rotation of the light chain domain (LCD), this is probably an unnecessary assumption.

CHAPTER 5 - Comparing SH1-SH2 BSL Crosslinked Rabbit S1 with Dicty S1dC

The results presented in CHAPTER 4 indicate that crosslinking SH1 and SH2 in rabbit S1 produces a weak binding, pre-force generating state on actin. The next step is to examine the effects in truncated *Dictyostelium discoideum* myosin II (S1dC) to see if these results are common to different isoforms of myosin II. In addition, we also examine the consequences of using an unsaturated BSL (as opposed to the saturated BSL used in CHAPTER 4) to determine if the high degree of orientational disorder is due, in part, to flexibility of the nitroxide ring. We find that using a more stable BSL reveals an ordered state in addition to the previously observed disorder of the head on actin. This observation further strengthens the hypothesis that the crosslinked state is in static equilibrium between weak and strong binding. Dicty S1dC exhibits a similar state, but is more heavily weighted towards the strong binding ordered state, consistent with previous observations (60).

5.1. Introduction

The results of CHAPTER 4 demonstrate that crosslinking the two reactive sulfhydryls (SH1 and SH2) in rabbit myosin S1 with a bifunctional spin label produces a state analogous to the previously reported weak binding state produced by crosslinking with pPDM (32-34). This study was novel in that the crosslinking agent was itself the probe for protein orientation and dynamics. We observed a weak binding state on actin that is as orientationally disordered as weak binding, but as dynamically slow as a strong binding, force generating state. These results suggested we had trapped an intermediate state that was on the cusp of undergoing a disorder to order transition.

While these results are indeed compelling, they suffer from a few weaknesses. One weakness results from the production of a crosslinked state which destroys any information about the biochemical state of myosin. This is problematic because we would like to be able to understand the coupling between biochemical and structural states in myosin. In spite of this, evidence exits that the presence of post hydrolysis analogs such as ADP.AlF_4 greatly enhances the rate of crosslinking SH1-SH2 in rabbit myosin (55). While we used ADP to increase the rate (and therefore the specificity) of crosslinking to be consistent with the previous studies of pPDM crosslinking, this gives some clue as to the coupling between biochemical and structural state pre-crosslinking.

Another weakness of the previous study is due to the amount of cysteines present in rabbit myosin S1, which affects the specificity of labeling. Indeed, it was found that BSL added in large molar excess (5 moles of BSL per mole of S1) of S1 was found to react almost completely (data not shown). Although the measurement of labeling specificity from the combination of high-salt ATPase and spin count (covered in detail in

CHAPTER 3) is compelling and leads us to believe we are only crosslinking SH1-SH2 with BSL, the presence of probes at other sites cannot be completely ruled out.

To address the limitations of the previous study, we have chosen to repeat these experiments in *Dictyostelium discoideum* myosin II, a myosin for which there exists a truncated, Cys-lite motor domain (Dicty S1dC). While wild type Dicty does not actually have an analogous SH1 cysteine, the structure of the SH1-SH2 helix shares a high degree of structural homology to the rabbit structure. By the addition of the appropriate SH1 and SH2 sites to the Cys-lite construct, the only cysteines that can be labeled in this system are those that we wish to crosslink, reducing concerns about labeling specificity. A previous study of this SH1-SH2 mutant found the same nucleotide induced crosslinking with pPDM, suggesting the same degree of structural flexibility and mechanical significance of this region in Dicty S1dC as in rabbit S1 (61).

While the use of Dicty resolves the difficulties of labeling specificity, it introduces the added variable of differences in coupling between biochemical and structural states of different myosin isoforms. A recent study of SH1 labeled Dicty and rabbit myosins found that while the Apo and ADP states show good structural similarity, the structural state due to post-hydrolysis ADP.P_i analogs, the state we believe we are trapping with crosslinking, shows substantial differences (60). With these differences in mind, we can develop a better understanding of the relationship between our trapped structural state in Dicty and rabbit SH1-SH2 and the biochemical states associated with the relative motions of the SH1-SH2 helix.

Finally, after the publication of the material in CHAPTER 4, we began using a different variant of BSL, one which has an unsaturated nitroxide ring, because it was

found to have a higher degree of stability and therefore acts as a better probe of orientation. We will do a direct comparison of the saturated (sBSL) and unsaturated (uBSL) probes in this crosslinking study.

5.2. Methods

Purification and Preparation of Mutant and Extracted Protein

Preparation of rabbit S1 was performed as described in CHAPTER 4. The SH1-SH2 mutant Dicty was produced following the methods of (60) and the initial DNA was based upon the Spudich Cys-lite full length S1 Dicty construct, which was a gift from Dr. Spudich. The purified proteins were stored in 60% glycerol at -80 °C until needed.

Preparation of Samples for EPR

Frozen rabbit S1 and Dicty SH1-SH2 were thawed on ice and then diluted 25x in labeling buffer (20mM MOPS, 50mM KCl, 3mM $MgCl_2$, 1mM EDTA, 1mM MgADP, pH 7.5). The diluted protein was then concentrated using Amicon Ultra 30kD MWCO membrane concentrators to facilitate the removal of glycerol. Samples were then reduced for 1hr in 5mM DTT. DTT was removed by the use of two spin columns equilibrated with labeling buffer. The protein concentration was then determined by UV absorbance: [rabbit S1] = $(A_{280}-A_{320})/(8.07 \times 10^4\ M^{-1}cm^{-1})$, [Dicty S1dC] = $(A_{280}-A_{320})/(6.13 \times 10^4\ M^{-1}cm^{-1})$. BSL was then added at a ratio of 1.1 moles of BSL per mole of unlabeled S1 and allowed to incubate on ice for 1 hr. Either uBSL (3,4-Bis-(methanethiosulfonylmethyl)-2,2,5,5-tetramethyl-2,5-dihydro-1H-pyrrol-1-yloxy Radical), or sBSL (Trans-3,4-bis-(methanethiosulfonylmethyl)-2,2,5,5-tetramethylpyrrolidin-1-yloxy Radical) was chosen as the crosslinking agent. Free label was removed through the use of two more spin columns equilibrated with the experimental buffer (40 mM MOPS, 2 mM $MgCl_2$, 1 mM

EGTA, pH 7.0). The samples were then concentrated one final time to a concentration of 20 - 50μM protein.

Rabbit psoas fiber bundles were prepared by dissecting glycerinated fiber bundles as described in CHAPTER 4. Fiber bundles of ~3mm in diameter and at least 2 cm in length were tied and threaded through 50μL wiretrol capillaries. Before EPR was performed, the tied fibers were incubated with spin labeled S1 for 1hr and then washed for 10 minutes with the experimental buffer via a peristaltic pump.

EPR

EPR of oriented muscle fibers were acquired with the muscle fiber axis in the parallel orientation with respect to the external magnetic field. This was accomplished by using a custom built Bruker TM110 cavity with holes bored through the sides to allow parallel sample alignment.

To facilitate buffer exchange and the removal of any unbound spin label, a peristaltic pump was attached to the muscle fiber capillary. The sample was maintained at the experimental temperature (4°C) by blowing dry nitrogen through the bottom of the TM cavity via a transfer dewar with the peristaltic flow off.

Fitting Oriented EPR Spectra

To fit an EPR spectrum to find the orientational distribution of the sample, the anisotropic matrix values of the electron g and the hyperfine T (equation 15) must be determined. In lieu of an actual crystal of the sample, these values can be obtained by finding the so called "effective tensor values." To obtain the effective values, the labeled S1 decorated muscle fiber is finely mined to remove any orientational order. This minced

sample is then placed in a flat cell and EPR is measured. The spectrum obtained is independent of sample orientation and is called a powder spectrum.

The powder spectrum was then fit using WACY, an in-house software application for the analysis and fitting of EPR spectra developed by Edmund Howard. The powder spectrum was fit by performing an iterative search on a grid defined by the following parameter space: g_{xx}, g_{yy}, g_{zz}, T_{xx}, T_{yy}, T_{zz}, Gaussian line width FWHM and Lorentzian line width FWHM. The range of each parameter was tuned by hand until an acceptable fit was found. These effective values were then applied to the fitting of oriented spectra.

The experimental spectra were baseline subtracted and normalized to their respective double integrals to make comparison of relative population weights between samples possible. Using the effective tensors found from the powder spectrum fit, the oriented spectra were fit two orientation populations by finding the mole fraction for each distribution, the angle between the nitroxide principle axis and the magnetic field (θ) and its Gaussian distribution. Since the T values for BSL were found to not be axially symmetric, it was useful to also fit the spectrum with an azimuthal angle (ϕ), also with a Gaussian distribution, though the sensitivity to ϕ is very small due the axial symmetry of myosin decoration of actin.

5.3. Results

Quantification of Labeling Specificity

As demonstrated in CHAPTER 3.4.2, the specificity of SH1-SH2 labeling in rabbit S1 can be calculated by measuring the K/EDTA and Ca/K high-salt ATPases in conjunction with the quantification of the number of spins per S1 molecule. Through this

analysis it was found that the specificity of uBSL and sBSL for SH1 and SH2 in rabbit S1 were essentially equivalent and preferentially crosslinked the cysteines (***Table 4***).

Table 4: sBSL vs uBSL labeling specificity in rabbit S1

Sample	NS labeling	SH1 Specificity	SH1-SH2 specificity
uBSL-S1	0.12	0.00	0.87
sBSL-S1	0.06	0.00	0.94

While the high-salt ATPase behavior of Dicty S1dC is considerably less characterized as compared to rabbit S1, previous measurement of the effect of crosslinking SH1-SH2 in mutant Dicty found a reduction of Actin activated ATPase as compared to unlabeled SH1-SH2 Dicty, but only in the presence of ADP (61). This behavior is consistent with the observed killing of high-salt ATPase activity seen in rabbit and the necessity of nucleotide to enable the cysteines to be within a crosslinkable distance. The observed Ca/K ATPase of unlabeled SH1-SH2 Dicty was 5.4 s^{-1} per myosin head, consistent with previously reported values (60). The addition of 1.1 moles of uBSL per mole of SH1-SH2 Dicty reduced the Ca/K ATPase by 97% suggesting complete reaction with SH1-SH2. Spin counting reveals a spin to protein ratio of 1.04. The reduction of Ca/K ATPase in conjunction with a one to one labeling ratio strongly suggest that uBSL completely reacts and crosslinks SH1-SH2 in Dicty S1dC.

Crosslinking SH1-SH2 with uBSL and sBSL

The resulting spectra of rabbit S1 labeled with either the unsaturated BSL (uBSL) or saturated BSL (sBSL) reveal a stark difference in orientational distributions when placed on oriented muscle fibers (**Fig. 22**). Comparison of oriented sBSL-S1 with the results presented in CHAPTER 4, **Fig. 18**, presents an essentially equivalent level of orientational disorder ($\Delta\theta' \geq 90°$). In contrast, the spectrum of uBSL-S1 on oriented fibers yields a two component spectrum, with 82 ± 5% of the spectrum being attributed to a disordered orientation with $\Delta\theta' \geq 90°$ and 18 ± 5% of the spectrum being an ordered population with $\theta' = 15.0° \pm 0.3°$ and $\Delta\theta' = 9.8° \pm 0.8°$.

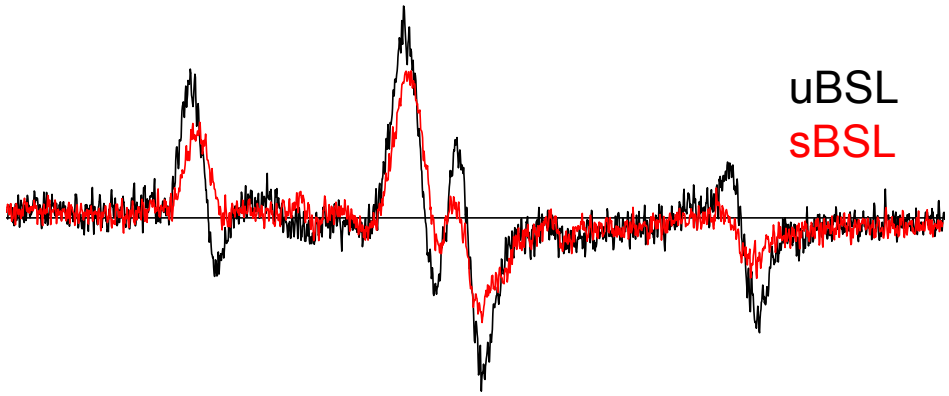

Fig. 22: uBSL vs sBSL on rabbit S1
Tied fiber bundles decorated with spin-labeled S1, aligned parallel in a capillary to the external magnetic field. The same preparation of rabbit S1 was labeled with either the unsaturated BSL (uBSL, black) or the saturated BSL (sBSL, red).

EPR of uBSL Labeled Rabbit S1 and Dicty S1dC

Rabbit S1 and Dicty S1dC that have SH1-SH2 crosslinked with uBSL on oriented muscle fibers display spectra composed of essentially identical orientational components (**Fig. 23**). The relative mole fraction of these components, on the other hand, is quite different between these two isoforms. As reported above, in the parallel orientation rabbit S1 displays an 82 ± 5% population with at least 90° of orientational disorder and a 12 ± 5% population with θ' = 15.0° ± 0.3° and $\Delta\theta'$ =9.8° ± 0.8°. Dicty S1dC exhibits these exact same orientational distributions, but the relative populations of each component are significantly different: 61 ± 5% ordered and 39 ± 5% disordered (**Table 5**).

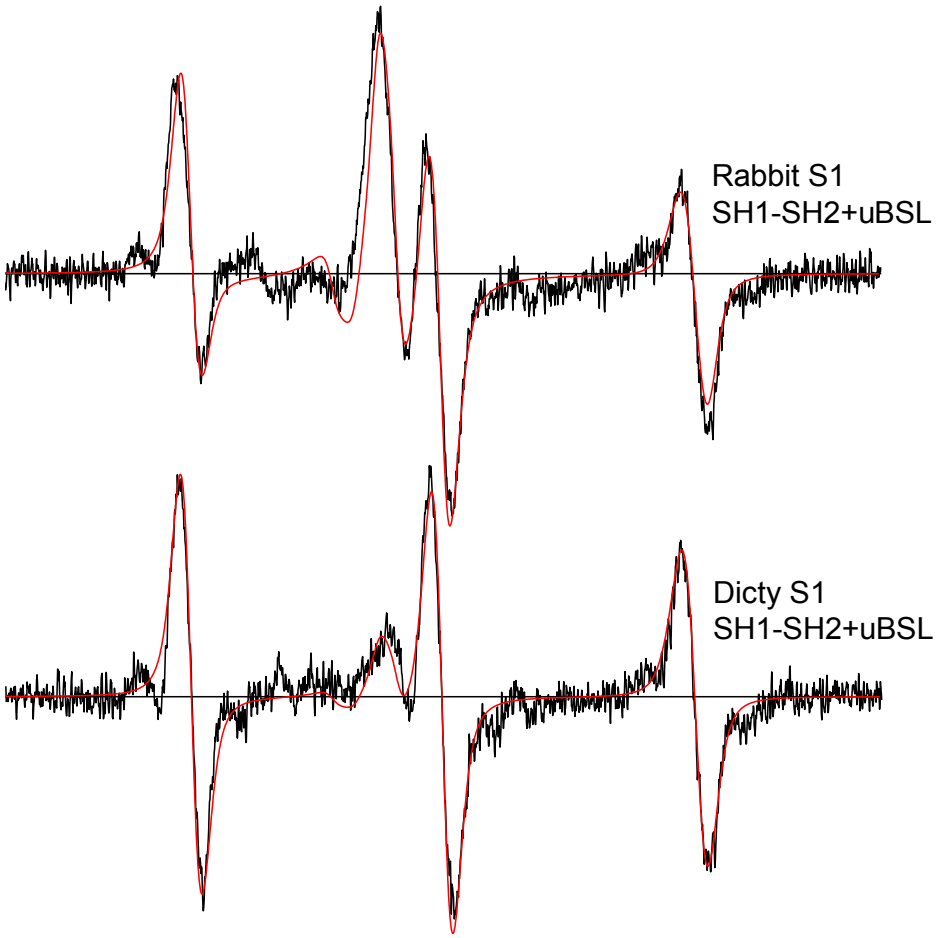

Fig. 23: Crosslinked rabbit S1 vs Dicty S1dC
Spectra of muscle fibers decorated with SH1-SH2 rabbit S1 or Dicty S1dC in the parallel orientation. Experimental spectra (black) are superimposed with the fit (red) to two orientation populations.

Table 5: Crosslinked rabbit S1 vs. Dicty S1dC

Sample	Ordered Fraction	Disordered Fraction
Rabbit SH1-SH2	0.18 ± 0.5	0.82 ± 0.5
Dicty SH1-SH2	0.61 ± 0.5	0.39 ± 0.5

Orientation of ordered component was $\theta' = 15.0° \pm 0.3°$ with $\Delta\theta' = 9.8° \pm 0.8°$. Disorder was $\Delta\theta' \geq 90°$

5.4. Discussion

Summary of Results

High-salt ATPases of rabbit SH1-SH2 crosslinked with BSL reveal a lack of activity characteristic of an S1 that is modified at both SH1 and SH2 simultaneously. In conjunction with spin counting, we see that BSL is highly specific for SH1 and SH2 and that the modification is accomplished by the formation of a crosslink between the sulfhydryls, rather than a monofunctional modification at each site. While not nearly as characterized as rabbit S1, high-salt Ca/K ATPase of SH1-SH2 Dicty S1dC also reveals a complete reduction of ATPase that suggests, with the high labeling efficiency revealed by spin counting, that BSL crosslinks SH1-SH2.

In contrast to the results presented in CHAPTER 4, where sBSL crosslinked rabbit S1 shows near complete orientational order, the results presented here indicate that both rabbit and Dicty S1dC crosslinked with uBSL exist in a state of static equilibrium between a state of orientational order and orientational disorder. Despite being different isoforms of S1, the characteristics of these two states are identical: the disordered populations has $\Delta\theta' \geq 90°$ and the ordered state shows an orientation of $\theta' = 15.0° \pm 0.3°$ and $\Delta\theta' = 9.8° \pm 0.8°$. The relative population of these states, though, differs between isoforms, with rabbit S1 being skewed towards disorder and Dicty S1dC being skewed towards the ordered population.

Interpretation of Results

The conclusion presented in CHAPTER 4 was that crosslinking SH1 and SH2 with sBSL produced a unique weak binding state on actin that had orientational characteristics of weak binding but dynamical characteristics of strong actin binding.

Coupled with the observation that nucleotide (in this case ADP), shifted the specificity towards that of complete crosslinking, we concluded that the SH1-SH2 crosslinking trapped a state intermediate between the weak-binding post-hydrolysis A.M'.D.P state and the strong binding, rigor like A.M'.D state.

In this study, our results using the more stable uBSL strengthen that previous conclusion by indicating that the crosslinked probe exists in equilibrium between static order and static disorder, strengthening the conclusion that the trapped state is on the cusp of making an order to disorder transition. Curiously, uBSL crosslinked Dicty SH1-SH2 shows an identical set of two states, but is biased towards the ordered strong binding state. This observation demonstrates that while rabbit and Dicty S1dC undergo the identical order to disorder transition, Dicty is shifted towards order consistent with the observation that phosphate analog release, and therefore the transition from weak to strong, is faster in Dicty than in rabbit (62).

Relationship to Previous Results

A recent study made a direct comparison between Dicty S1dC and rabbit S1 and sought to characterize the correspondence between structural states and biochemical states, particularly those of the pre- and post-hydrolysis analogs (63). The findings of this study were that both Dicty and rabbit shared distinct structural states, namely M* (post-powerstroke, near-rigor) and M** (pre-powerstroke), but the coupling between those states differed depending on the nucleotide analog present. With the post-hydrolysis analog ADP.AlF_4, for example, they found that rabbit S1 exhibited an 85% population of pre-powerstroke heads and 15% near rigor heads. Dicty S1dC, on the other hand exhibited a 28% population of pre-powerstroke heads and 72% near-rigor heads.

As presented in CHAPTER 4, the data suggested a trapped state consistent with a post-hydrolysis, near-rigor state. With the higher orientational resolution provided by the more stable uBSL, we see that this hypothesis is further supported by the results of (63) in that the relative populations of pre-powerstroke (but post-hydrolysis) heads to near-rigor heads agree quite well with the results presented in this study.

Alternative Explanations

As demonstrated in CHAPTER 3, uBSL attached to a helix at residues i and i+4 exhibits two different label conformations but with similar degrees of order, $\Delta\theta' \sim 10°$. In this study we also see two populations, but each with drastically different degrees of orientational order. It would seem highly unlikely, therefore, that the relative populations are due merely to spin label attachment orientation.

As with the previous study (CHAPTER 4), the possibility remains that the observed order/disorder is merely due to changes in the local spin environment and is not a measure of large domain orientation. Indeed, the measurements of (63) are reporting changes in spin label mobility due to local changes in the spin label environment. In this particular study, this can not be ruled out and will have to be addressed in a future study (see CHAPTER 7)

Implications for the WS State in Dicty and Rabbit

The additional resolution provided by uBSL yields further insight into the nature of the WS state created by crosslinking SH1-SH2. The presence of two components of drastically different orientational order suggests that the crosslinked state is in static equilibrium between the WS state described in CHAPTER 4, and a strong binding, rigor-like complex that is a post-hydrolysis state (**Fig. 24**).

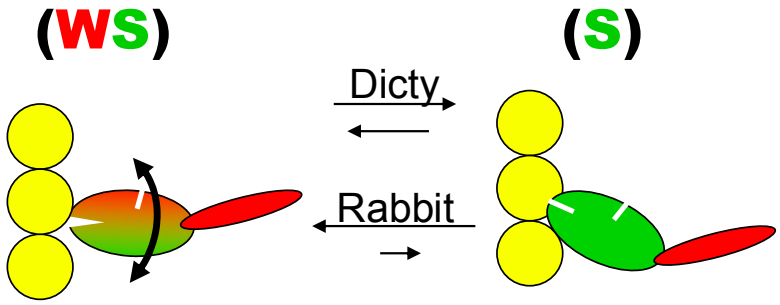

Fig. 24: Refinement of the WS state
Crosslinking SH1-SH2 creates an equilibrium between the previously reported WS (slow dynamics, disorder) state and a S (slow dynamics, ordered) post-hydrolysis rigor like state. Crosslinked rabbit S1 is skewed towards the WS state whereas Dicty S1dC tends towards the S state, consistent with Dicty's increased rate phosphate analog release, which suggests a faster W to S transition (62).

CHAPTER 6 - Probing the Effects of an FHC Point Mutation of Dicty Myosin Catalytic Domain Orientation

A previous study in smooth muscle myosin found that the addition of a single point mutation (R403Q) found in patients with Familial Hypertrophic Cardiomyopathy (FHC) caused orientational disorder in both the Apo and ADP states of actin bound heads, and affected the level of rotation of the lever arm induced by ADP binding (64). This finding is significant because it suggests that the macroscopic hypertrophy of the heart tissue may be caused by disorder at the microscopic level. In this study we seek to characterize the analogous mutation in Dicty S1dC, R397Q, utilizing the orientational sensitivity of BSL attached to the lower 50kD (L50kD) domain. We find that the R397 Dicty labeled on the L50kD domain has a high degree of orientational order and undergoes ~3° rotation in the presence of ADP. The R397Q mutation, in contrast to the previous study, shows practically the same orientation and rotation due to ADP as WT. This indicates the L50kD domain is rigidly coupled to actin, and that the observed disorder of the FHC heads and change in ADP induced lever arm rotation must be solely due to motion of the U50kD domain.

6.1. Introduction

Familial Hypertrophic Cardiomyopathy (FHC) is an inherited disease that, in part, results in an increased thickness of the left ventricular wall of the heart (65). One of the causes of FHC has been determined to be several (>29) missense mutations in the gene responsible for the expression of cardiac myosin (66). A particularly lethal member of those mutations which often results in sudden death, occurs in a well conserved region of myosin called, for obvious reasons, the cardiomyopathy (CM) loop (**Fig. 25**). In humans this mutation manifests as a glutamine (Q) at residue 403 in place of the native arginine (R). In other myosin isoforms, such as Dicty myosin, smooth muscle myosin and chicken skeletal myosin, the equivalent mutation is R397Q, R406Q and R405Q respectively.

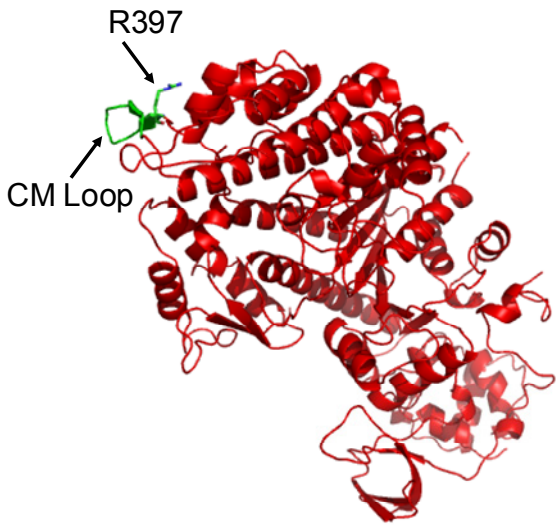

Fig. 25: The cardiomyopathy (CM) loop
1FMV crystal structure of Dicty S1dC. The CM loop (green) spans residues 397-407.

Aside from the obvious disease implication, study of this mutation's effect on myosin has revealed much about the mechanism of the actomyosin complex. The high degree of conservancy found in the cardiomyopathy loop amongst various myosin isoforms suggests it plays an important role in the coupling of myosin to actin. A previous study attempting to fit the myosin crystal structure into the EM reconstructions of actin decorated with myosin found that the crystal structure fit to the observed densities inadequately without manipulation (5). To achieve a reasonable fit, the U50kD domain of myosin was forced to rotate, closing the nucleotide binding pocket and bringing the cardiomyopathy loop into direct contact with actin. The cardiomyopathy loop itself is composed of a series of hydrophobic residues that, when deleted, completely eliminate the ability of myosin to form a strong binding complex with actin even in the absence of nucleotide (67).

Disruption by the R to Q mutation of such a crucial component in the formation of the actomyosin complex has been found to have a direct effect on the rate of actin activated ATPase, strength of actin binding and the rate of actin displacement in motility assays, though the direction of the effect (gain of function or loss of function) is not consistent amongst different studies. Measurements in Dicty myosin found that the R397Q mutation reduced the rate of actin-activated MgATPase (V_{max}) by 77% that of wild type, decreased the strength of actin binding (K_m) by a factor of 2.2 and reduced the sliding velocity of actin on glass plates decorated with mutant myosin (68). A later study in the same system found equivalent weakening of actin binding, but saw no affect on the rate of ATP hydrolysis or on sliding velocity (69). Studies in different systems, such as rat α-cardiac myosin have also found similar results (70,71).

It would seem that the loss of myosin function is a common feature amongst the various isoforms of this point mutation, but more recent data have revealed effects consistent with a gain in myosin function. Single molecule measurements of mutant myosin found similar levels of force and displacement to wild type, but a decrease in the overall actin attachment time (72,73). Measurements of actin sliding velocity in both of these studies showed a 30-40% increase. How can these dramatic differences be resolved? The presence of denatured protein (rigor-like dead heads) in an ensemble measurement of sliding velocity may have a confounding effect on the functional protein (73). In addition, expressed protein typically has a rapid rate of degradation at low yields, resulting in lower than normal activity (72).

While the effects of the R to Q mutation on biochemical activity and mechanical behavior point towards a disruption of actomyosin interaction, they do not reveal the specific structural mechanisms that the mutation is disrupting. Computer simulations of this region using the chicken S1 structure reveal that, when bound to actin, the cardiomyopathy loop is a flexible structure and that R405 forms a strong salt bridge with E605 (74). The R405Q mutation breaks this salt bridge, and the flexible cardiomyopathy loop forms a rigid β-sheet, potentially destabilizing the U50kD domain's interaction with actin.

A direct measurement of the structural effects of the R to Q mutation was observed by cryo EM of actin filaments decorated with smooth muscle myosin (64). The mutation dramatically disrupted the classical arrow headed pattern of rigor heads on actin, instead yielding disorder of the head and light chain comain orientation with ~15° standard deviation. While the attached heads still exhibited ADP induced rotation of the light chain domain, the mutation reduced the amplitude of this rotation.

What are the structural implications of the observed disorder caused by the R to Q mutations? Is the observed orientational disorder in the head and light chain domain caused by a disruption of the U50kD domain, or does the mutation cause disorder in the L50kD domain as well? These are questions that EPR of bifunctionally labeled Dicty myosin are best suited to answer.

6.2. Methods

Preparation of Samples and Collection of Spectra

The purification of mutant protein, the preparation of samples and the collection of EPR were performed following the methods of CHAPTER 5.

Modeling of BSL Attachment to the L50 Domain

An energy minimized structure of uBSL, including the disulfide bond and cysteine S_γ, was obtained by Bengt Svensson. Using this energy minimized structure, the spin label was attached to residues A639C.A643C of the Apo structure of Dicty S1dC (1FMV, (4)) using the program Accelrys DS version 1.7. Briefly, the spin label was introduced to the structure and manually arranged in a similar orientation to that of the previously reported crystal structure (10). Bonds were created between the C_β's of the residues 639 and 643 and the S_γ's of uBSL, effectively making residues 639 and 643 cysteines. The hand drawn structure was then optimized by allowing the program to correct the bond lengths and geometries of the attached probe and the cysteine C_β's and S_γ's. The second structure of uBSL attachment was found by rotating the initial uBSL structure by ~90° about the Nitroxide N-O bond, followed by attachment and optimization following the above procedure.

Modeling Protein Orientation from EPR data

The 1FMV structure shares an incredible degree of structural homology with the Rayment chicken skeletal myosin S1 Apo structure (2MYS, (2)), which can be observed by using the web based utility at http://cl.sdsc.edu/ce/ce_align.html. Utilizing this fact, the uBSL docked 1FMV structures were fit (using the web based utility) into a model for the nucleotide free actomyosin complex (1ALM, (75)). Coordinates for the spin label

principle axis (z) were determined by finding the normal to the nitroxide ring, utilizing the bonds between N-C_2 and N-C_5 as vectors for the plane. The x axis for the nitroxide coordinate system was defined as the N-O bond of the nitroxide. With the spin label principle axis defined in a coordinate space containing both actin and myosin, it is then possible to compare the spin label models with measured spectra (the angle between the spin label axis and a vector running the length of the actin filament) and determine how the measured angles relate to the angle that the uBSL labeled helix makes with the actin filament.

6.3. Results

uBSL has Two Conformations on the L50 Domain Helix

The spectrum of uBSL on residues 639 and 643 of Dicty S1dC on actin in the absence of nucleotide (Apo) reveals two, well defined and distinct orientation components (**Fig. 11**). Analysis of these two components by utilizing the effective tensors found from a randomized sample yield a dominant population (68 ± 5%) with $\theta' = 28.1° \pm 0.3°$ and $\Delta\theta' = 11.6° \pm 0.8°$ and a minor population with $\theta' = 78.3° \pm 0.3°$ and $\Delta\theta' = 10.3° \pm 0.8°$. Since the orientation of myosin on actin is extensively documented to be well defined and stable in rigor on actin (76-78), the only reasonable conclusion to the observed populations of similar order separated by ~50° is that uBSL can bind to the helix at residues i and i+4 in two unique, yet equally stable conformations (**Fig. 26**).

Simulations of these two spin label conformations on the actin bound 1FMV Dicty structure yields two orientations of the nitroxide ring normal (which is the spin label principle axis) with respect to the long axis of the actin filament (**Fig. 27**). For the structure represented in **Fig. 26** A (Structure 1), the spin label principle axis makes an angle of $\theta' = 24°$. For the structure represented in **Fig. 26** B (Structure 2), the spin label principle axis makes an angle of $\theta' = 76°$. Both of these modeled structures are in excellent agreement with the angles determined from the measured spectra.

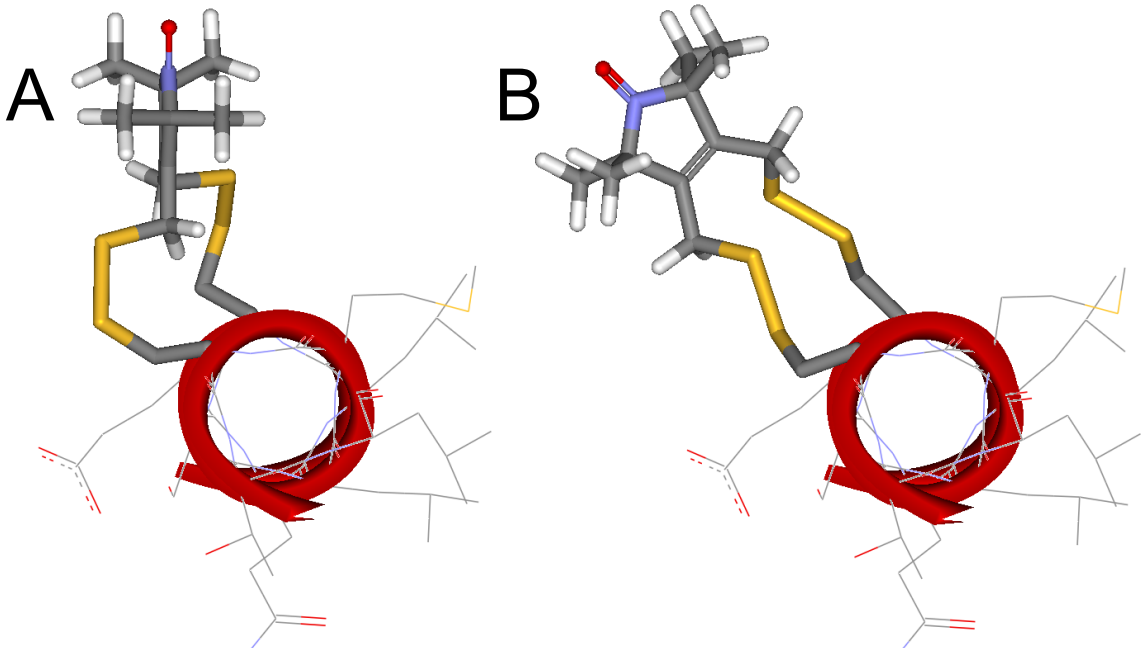

Fig. 26: uBSL conformations on a helix
The spin label principle axis is 88° (A, Structure 1) and 18° (B, Structure 2) with respect to a vector running the length of the helix core.

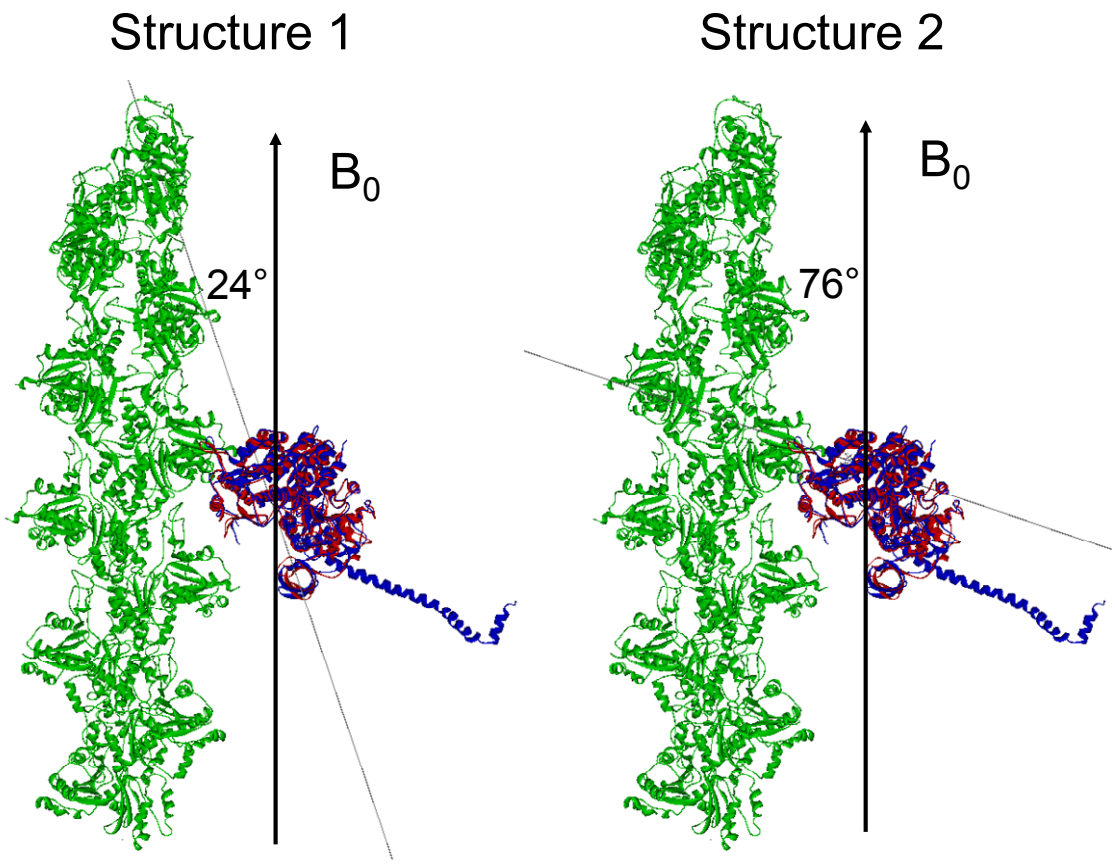

Fig. 27: Simulating uBSL's orientation on actin bound A639C.A643C Dicty S1dC**.**
Mutant Dicty S1dC (red) is aligned with the chicken skeletal S1 (blue), which is docked on actin (green). The two possible spin label conformations are shown with their respective principle axes drawn with respect to the external magnetic field (B_0), and thus the actin long access when muscle fibers are aligned in the parallel orientation.

ADP Induced Fotation of the L50 domain

The addition of 1mM ADP to the decorated muscle fibers causes a small, but distinct change in the observed spectrum (**Fig. 28)**. By inspection, it is clear that all of the change is found in the component of the spectrum due to Structure 1. Analysis of the spectrum reveals a rotation of 3.2° from the Apo state ($\Delta\theta'$ =29.3° ± 0.3°) to the ADP state (θ' =26.1° ± 0.3°). The observed change in angle is accompanied by no change in orientational disorder (**Table 6**).

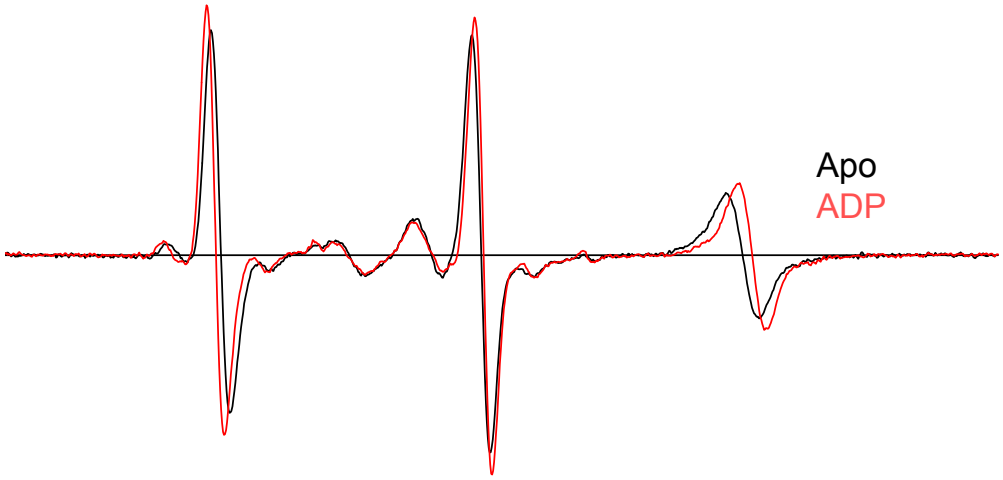

Fig. 28: ADP induced rotation of the L50kD domain
Spectra of A639C.A643C Dicty S1dC labeled with uBSL were recorded with the muscle fiber axis parallel to the external magnetic field. Spectra were recorded in the absence (black) and presence (red) of 1mM MgADP.

Table 6: ADP induced rotation of the L50kD domain

Sample	Apo	ADP
Structure 1	**68 ± 5%**	
θ'	29.3° ± 0.3°	26.1° ± 0.3°
$\Delta\theta'$	11.6° ± 0.8°	11.6° ± 0.8°
Structure 2	**32 ± 5%**	
θ'	78.3° ± 0.3°	78.3° ± 0.3°
$\Delta\theta'$	10.3° ± 0.8°	10.3° ± 0.8°

Effect of the R397Q on L50 Domain Orientation

EPR of R397Q Dicty labeled at residues 639 and 643 with uBSL reveals a spectrum with a near identical orientation to that of Dicty labeled at the equivalent sites but lacking the functional mutation (**Fig. 29**). Addition of 1mM ADP via peristaltic flow to the actin bound mutant protein also yields the same level of orientation as observed in protein without the functional mutation. A qualitative inspection of the spectra reveal subtle changes in lineheight, indicating slight changes in orientational disorder, but quantitation of these changes yields results within the error of the fitting technique.

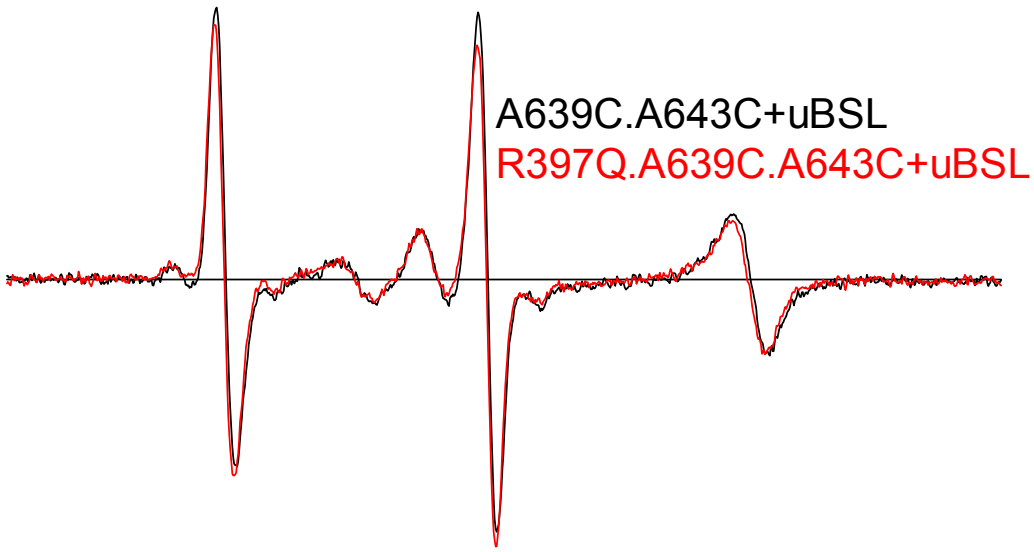

Fig. 29: EPR R397Q Dicty labeled with uBSL at A639C.A643C
Spectra of rabbit psoas fibers decorated with Dicty S1dC labeled at residues 639 and 643 with uBSL (black) and the equivalent protein with the R397Q mutation (red). Spectra were acquired at 4°C with the muscle fibers aligned (parallel) with the external magnetic field.

6.4. Discussion

Summary of Results

The spectra of muscle fibers decorated in the absence of nucleotide with Dicty S1dC labeled at residues A639C.A643C with uBSL reveal line shapes that are characteristic of a rigidly attached, well oriented probe. Analysis of the orientation reveals a two component spectrum: a dominant component with θ' = 28.1° ± 0.3° and $\Delta\theta'$= 11.6° ± 0.8° and a minor component ~50° away with a similar level of disorder. By docking uBSL to the crystal structure of Dicty, the best interpretation to these results is that the spin label adopts two conformations on the labeled helix, one with the principle axis perpendicular (Structure 1) to the helix axis and one parallel (Structure 2).

The addition of ADP to the decorated fibers induces a small but resolvable rotation in the spectra (~3°), with the spin label axis becoming more aligned with the external magnetic field. This change is accompanied by no change in the amount of angular disorder, indicating a stable, rigid body rotation. Surprisingly, the change in the spectra is only found in the lineshapes that are attributed to Structure 1.

The addition of the functional mutation R397Q to the uBSL labeled Dicty adds no discernable difference to the measured orientation of the probes when compared with labeled Dicty lacking the functional mutation. Similarly, the addition of ADP also induces the small rotation in the L50 domain that is resolved by the Structure 1 component of the spectrum.

Interpretation of Results

The remarkable amount of orientational order found in the spectra of uBSL labeled A639C.A643C Dicty S1dC in the rigor state demonstrates the spin label's rigid coupling to the protein backbone and therefore its ability to resolve small changes in orientation. Added to this rigid coupling is the presence of two distinct spin label orientations on the labeled helix. While it does complicate the analysis by requiring a two component fit, it allows further sensitivity (for this labeling site and preparation) to structural changes at this particular site: θ', $\Delta\theta'$ measured by Structure 1 are sensitive to twisting of the helix about its axis and θ', $\Delta\theta'$ measured by Structure 2 are sensitive to changes in non-azimuthal tilt of the helix axis with respect to the actin axis (**Fig. 30**). Whether this is a feature common to all i and i+4 sites on the myosin heavy chain will require further study.

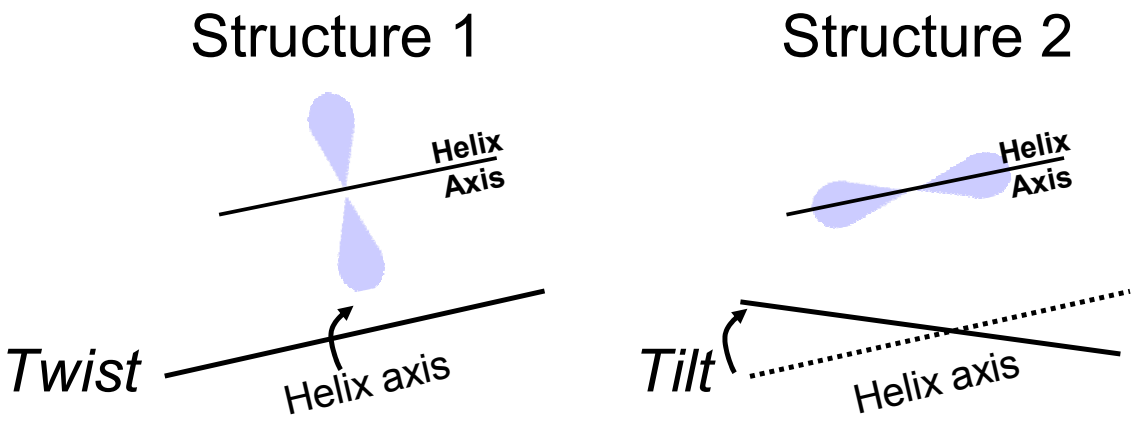

Fig. 30: Sensitivity of the labeling structures to helix motion
The different labeling structures (Structures 1 and 2, shown in **Fig. 26**) are sensitive to different motions of the labeled helix axis. The blue cartoon represents the electron cloud, with the spin label principle axis (z) running its length. This relationship is not true for all potential labeling sites due to labeled helix geometry with respect to the actin axis.

As discussed in the results, the addition of 1mM ADP causes a distinct change in orientation in the Structure 1 part of the spectrum, but virtually no change in the Structure 2 component. From this we can conclude that ADP induces no change in helix tilt with respect to actin, but causes a twist of the helix about its axis. Modeling of the effect of helix rotation on the angle the spin label principle axis makes with actin yields that the direction of this rotation is towards the 50 kD cleft (**Fig. 31**).

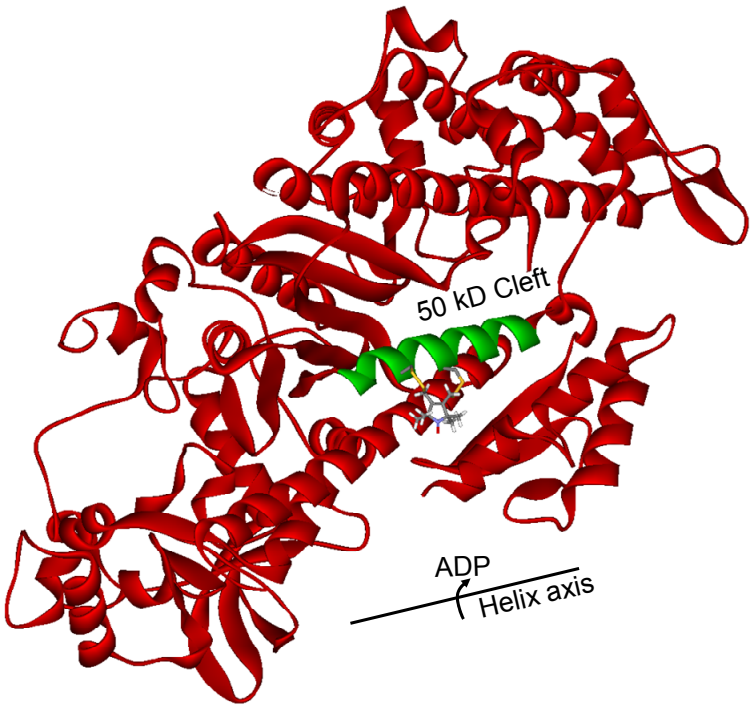

Fig. 31: Schematic of ADP induced rotation of the L50
Dicty S1dC labeled at residues A639C.A643C with uBSL with the spin label in the Structure 1 orientation. The labeled helix is indicated in green. The presence of ADP causes rotation of the helix about its long axis towards the 50kD cleft.

The addition of the functional mutation R397Q, surprisingly, has no measurable effect on the tilt, twist or level of disorder of this helix. The ability of ADP to still induce a conformational change suggests that any functional effects must be limited to the U50kD domain. These results directly show that the L50kD domain is one of the structural elements involved in strong actin binding, even in states that have been demonstrated to indicate characteristics of weak binding.

Relationship to Previous Results

While, as far as the author knows, this is the first direct measurement of the orientation of this helix and its sensitivity to ADP, previous results have demonstrated that some level of motion is expected to occur. Indeed, relative motion of the U50-L50kD domains remains one of the most widely studied topics in the field of myosin. Recent measurements of distances between the U50-L50kD domains observe two distance populations on actin (79). While the results presented here indicate a single, well defined orientation of this helix in the L50kD domain, they are not necessarily contradictory because the U50kD domain could be moving relative to the L50kD. In addition, this site has very little sensitivity to axial motion about the actin axis, so any changes in azimuthal orientation would be difficult to resolve.

Previous examination on the effect of ADP on domain motion was found by comparing Cryo EM reconstructions of smooth muscle S1 (80). In this study, they found an increase in structural density around the L50kD domain in the Apo state as compared to the ADP state, suggesting a motion of the domain towards to 50kD cleft, thereby closing it, when nucleotide is bound. This observation is in direct agreement with our observation of a rotation of the labeled helix toward the cleft upon ADP binding. It

should be pointed out that these observations can only be made in a system containing both myosin and actin, as comparison of the ADP (1MMA, (81)) bound and Apo (1FMV) Dicty crystal structures in the absence of actin reveal no change in this region.

Although a dramatic increase of orientational disorder was hypothesized to be observed in the L50kD domain based upon the previous observations from cryo EM (64), the lack of change observed is not entirely surprising based on the knowledge that the L50kD domain forms a strong interaction with actin. Indeed, the authors of the study assumed this fact when modeling the orientational disorder induced by the functional mutation. It should be noted, though, that the labeled helix is directly connected to a nearby β-sheet that has been shown to be coupled to the state of the nucleotide pocket (82), and that this β sheet may act as the hinge enabling cleft closure (5). This could indicate the degree of disorder present in the U50kD domain may be relatively small compared to the observed disorder that is propagated to the light chain domain. Alternatively, the previously reported disorder (64) may be unique to the choice of myosin isoform used, and thus may not be observed in Dicty S1dC. Direct measurement of the orientation and disorder of the U50kD are needed to test these hypotheses.

CHAPTER 7 - Discussion and Future Directions

The bifunctional spin label has proven to be an exceptionally powerful tool for probing the orientation and dynamics of muscle myosin due to EPR's high resolution capabilities for measuring each. When used to crosslink the reactive sulfhydryls (SH1 and SH2) in rabbit and engineered Dicty myosin, BSL traps a weak binding state that is consistent with a post-hydrolysis myosin that is on the threshold of force generation. When placed on a helix and residues i and i+4, BSL can provide *in vitro* measurement of individual secondary structure elements that rivals techniques, such as cryo EM, in its level of sensitivity and surpasses them in the ability to perform experiments on systems in their physiological environments.

With regard to the weak binding state produced by crosslinking SH1-SH2, the possibility remains that the observed orientational distributions merely represent local order and disorder of the SH1 helix. Now that crosslinked Dicty SH1-SH2 has been characterized and found similar to rabbit S1, we can begin to answer this question. By placing additional bifunctional labeling sites (such as residues A639C.A643C on the L50kD domain or other stable helices on the U50kD domain), we will be able to distinguish between local disordering of the SH1 helix and global disordering of whole domains on actin. Simultaneous measurement of different domains and crosslinking SH1-SH2 will allow us to better understand this helix's role in the formation of the strong binding state on actin and the transmission of information from the nucleotide binding pocket to the force generating regions of myosin.

The presence of two spin label orientation populations on a single bifunctional labeling site adds further sensitivity to conformational changes of domains, at the

expense of spectral feature overlap. Whether these two populations appear in all examples of i and i+4 labeling remains to be seen. New, stable helices on the myosin head need to be explored to see how this behavior depends on local secondary structure, and if Structure 1 is always the dominant component. Molecular dynamics simulation of the probe attached to a helix in myosin will also help address this phenomenon.

The R397Q mutation on the cardiomyopathy loop, like the crosslinking of SH1-SH2, has the potential to reveal how myosin transitions from a weak to strong binding state on actin. The measurements of the L50kD domain demonstrate that this domain is rigidly attached to actin, in spite of the observed instability introduced by this mutation. The addition of new BSL labeling sites on the U50kD domain will reveal whether the observed disorder is due to instability in this domain, or that the disorder is propagated to the light chain domain by some other mechanism.

Bibliography

1. Bagshaw, C. R. 1993. Muscle Contraction: Chapman & Hall.

2. Rayment, I., W. R. Rypniewski, K. Schmidt-Base, R. Smith, D. R. Tomchick, M. M. Benning, D. A. Winkelmann, G. Wesenberg, and H. M. Holden. 1993. Three-dimensional structure of myosin subfragment-1: a molecular motor. Science 261:50-58.

3. Huxley, A. F. and R. M. Simmons. 1971. Proposed mechanism of force generation in striated muscle. Nature 233:533-538.

4. Bauer, C. B., H. M. Holden, J. B. Thoden, R. Smith, and I. Rayment. 2000. X-ray structures of the apo and MgATP-bound states of Dictyostelium discoideum myosin motor domain. J Biol Chem 275:38494-38499.

5. Holmes, K. C., I. Angert, F. J. Kull, W. Jahn, and R. R. Schroder. 2003. Electron cryo-microscopy shows how strong binding of myosin to actin releases nucleotide. Nature 425:423-427.

6. Houdusse, A., V. Kalabokis, D. Himmel, A. Szent-Gyorgyi, and C. Cohen. 1999. Atomic structure of scallop myosin subfragment S1 complexed with MgADP: a novel conformation of the myosin head. Cell 97:459-470.

7. Baker, J. E., I. Brust-Mascher, S. Ramachandran, L. E. LaConte, and D. D. Thomas. 1998. A large and distinct rotation of the myosin light chain domain occurs upon muscle contraction. Proc Natl Acad Sci U S A 95:2944-2949.

8. Thomas, D. D., D. Kast, and V. L. Korman. 2009. Site-Directed Spectroscopic Probes of Actomyosin Structural Dynamics. Annu. Rev. Biophys. 38:347-369.

9. Campbell, I. D. and R. A. Dwek. 1984. Biological Spectroscopy: Benjamin-Cummings.

10. Fleissner, M. 2005. X-ray Structures of Nitroxide Side Chains in Proteins: A Basis for Interpreting Distance Measurements and Dynamic Studies by Electron Paramagnetic Resonance [PhD Thesis]. Los Angeles: UCLA.

11. Thompson, A. R., N. Naber, C. Wilson, R. Cooke, and D. D. Thomas. 2008. Structural dynamics of the actomyosin complex probed by a bifunctional spin label that cross-links SH1 and SH2. Biophys J 95:5238-5246.

12. Matta, J. J. 1994. Biochemical and Mechanical Effects of Spin Labeling Muscle Fibers [PhD Thesis]. Minneapolis: University of Minnesota.

13. Thomas, D. D., S. Ramachandran, O. Roopnarine, D. W. Hayden, and E. M. Ostap. 1995. The mechanism of force generation in myosin: a disorder-to-order transition, coupled to internal structural changes. Biophys J 68:135S-141S.

14. Taylor, K. A., H. Schmitz, M. C. Reedy, Y. E. Goldman, C. Franzini-Armstrong, H. Sasaki, R. T. Tregear, K. Poole, C. Lucaveche, R. J. Edwards, L. F. Chen, H. Winkler, and M. K. Reedy. 1999. Tomographic 3D Reconstruction of Quick-Frozen, Ca2+-Activated Contracting Insect Flight Muscle. Cell 99:421-431.

15. LaConte, L. E., J. E. Baker, and D. D. Thomas. 2003. Transient kinetics and mechanics of myosin's force-generating rotation in muscle: resolution of millisecond rotational transitions in the spin-labeled myosin light-chain domain. Biochemistry 42:9797-9803.

16. Thomas, D. D. and R. Cooke. 1980. Orientation of spin-labeled myosin heads in glycerinated muscle fibers. Biophys J 32:891-906.

17. Cooke, R., M. S. Crowder, and D. D. Thomas. 1982. Orientation of spin labels attached to cross-bridges in contracting muscle fibres. Nature 300:776-778.

18. Berger, C. L., E. C. Svensson, and D. D. Thomas. 1989. Photolysis of a photolabile precursor of ATP (caged ATP) induces microsecond rotational motions of myosin heads bound to actin. Proc Natl Acad Sci U S A 86:8753-8757.

19. Berger, C. L. and D. D. Thomas. 1993. Rotational dynamics of actin-bound myosin heads in active myofibrils. Biochemistry 32:3812-3821.

20. Berger, C. L. and D. D. Thomas. 1991. Rotational dynamics of actin-bound intermediates in the myosin ATPase cycle. Biochemistry 30:11036-11045.

21. Berger, C. L. and D. D. Thomas. 1994. Rotational dynamics of actin-bound intermediates of the myosin adenosine triphosphatase cycle in myofibrils. Biophys J 67:250-261.

22. Craig, R., L. E. Greene, and E. Eisenberg. 1985. Structure of the actin-myosin complex in the presence of ATP. Proc Natl Acad Sci U S A 82:3247-3251.

23. Walker, M., J. Trinick, and H. White. 1995. Millisecond time resolution electron cryo-microscopy of the M-ATP transient kinetic state of the acto-myosin ATPase. Biophys J 68:87S-91S.

24. Walker, M., H. White, B. Belknap, and J. Trinick. 1994. Electron cryomicroscopy of acto-myosin-S1 during steady-state ATP hydrolysis. Biophys J 66:1563-1572.

25. Takagi, Y., H. Shuman, and Y. E. Goldman. 2004. Coupling between phosphate release and force generation in muscle actomyosin. Philos Trans R Soc Lond B Biol Sci 359:1913-1920.

26. Smith, D. A. and J. Sleep. 2004. Mechanokinetics of rapid tension recovery in muscle: the Myosin working stroke is followed by a slower release of phosphate. Biophys J 87:442-456.

27. White, H. D., B. Belknap, and M. R. Webb. 1997. Kinetics of Nucleoside Triphosphate Cleavage and Phosphate Release Steps by Associated Rabbit Skeletal Actomyosin, Measured Using a Novel Fluorescent Probe for Phosphate. Biochemistry 36:11828-11836.

28. Prochniewicz, E., T. F. Walseth, and D. D. Thomas. 2004. Structural dynamics of actin during active interaction with myosin: different effects of weakly and strongly bound myosin heads. Biochemistry 43:10642-10652.

29. Werber, M. M., Y. M. Peyser, and A. Muhlrad. 1992. Characterization of stable beryllium fluoride, aluminum fluoride, and vanadate containing myosin subfragment 1-nucleotide complexes. Biochemistry 31:7190-7197.

30. Pate, E. and R. Cooke. 1988. Energetics of the actomyosin bond in the filament array of muscle fibers. Biophys J 53:561-573.

31. Fajer, P. G., E. A. Fajer, N. J. Brunsvold, and D. D. Thomas. 1988. Effects of AMPPNP on the orientation and rotational dynamics of spin-labeled muscle cross-bridges. Biophys J 53:513-524.

32. Greene, L., J. Chalovich, and E. Eisenberg. 1986. Effect of nucleotide on the binding of N,N'-p-phenylenedimaleimide-modified S-1 to unregulated and regulated actin. Biochemistry 25:704-709.

33. Chalovich, J., L. Greene, and E. Eisenberg. 1983. Crosslinked myosin subfragment 1: a stable analogue of the subfragment-1.ATP complex. Proc Natl Acad Sci USA 80:4909-4913.

34. Bobkov, A. and E. Reisler. 2000. Is SH1-SH2-cross-linked myosin subfragment 1 a structural analog of the weakly-bound state of myosin? Biophysical journal 79:460-467.

35. Wells, J. and R. Yount. 1979. Active site trapping of nucleotides by crosslinking two sulfhydryls in myosin subfragment 1. Proc Natl Acad Sci USA 76:4966-4970.

36. Burke, M. and E. Reisler. 1977. Effect of nucleotide binding on the proximity of the essential sulfhydryl groups of myosin. Chemical probing of movement of residues during conformational transitions. Biochemistry 16:5559-5563.

37. Dalbey, R., J. Weiel, and R. Yount. 1983. Förster energy transfer measurements of thiol 1 to thiol 2 distances in myosin subfragment 1. Biochemistry 22:4696-4706.

38. Bagshaw, C. R. 1993. Muscle Contraction. New York: Chapman & Hall. 155 p.

39. Prochniewicz, E., D. A. Lowe, D. J. Spakowicz, L. Higgins, K. O'Conor, L. V. Thompson, D. A. Ferrington, and D. D. Thomas. 2008. Functional, structural, and chemical changes in myosin associated with hydrogen peroxide treatment of skeletal muscle fibers. Am J Physiol Cell Physiol 294:C613-626.

40. Barnett, V. A. and D. D. Thomas. 1987. Resolution of conformational states of spin-labeled myosin during steady-state ATP hydrolysis. Biochemistry 26:314-323.

41. Lanzetta, P. A., L. J. Alvarez, P. S. Reinach, and O. A. Candia. 1979. An improved assay for nanomole amounts of inorganic phosphate. Anal Biochem 100:95-97.

42. Prochniewicz, E. and D. D. Thomas. 2001. Site-specific mutations in the myosin binding sites of actin affect structural transitions that control myosin binding. Biochemistry 40:13933-13940.

43. Geeves, M. A., T. E. Jeffries, and N. C. Millar. 1986. ATP-induced dissociation of rabbit skeletal actomyosin subfragment 1. Characterization of an isomerization of the ternary acto-S1-ATP complex. Biochemistry 25:8454-8458.

44. Squier, T. C. and D. D. Thomas. 1986. Methodology for increased precision in saturation transfer electron paramagnetic resonance studies of rotational dynamics. Biophys J 49:921-935.

45. Fajer, P. G., R. L. H. Bennett, C. F. Polnaszek, E. A. Fajer, and D. D. Thomas. 1990. General method for multiparameter fitting of high-resolution EPR spectra using a simplex algorithm. J. Magn. Res. 88:111-125.

46. Karim, C. B., Z. Zhang, and D. D. Thomas. 2007. Synthesis of TOAC spin-labeled proteins and reconstitution in lipid membranes. Nat Protoc 2:42-49.

47. Sekine, T. and W. W. Kielley. 1964. The enzymic properties of N-ethylmaleimide modified myosin. Biochim Biophys Acta 81:336-345.

48. Reisler, E., M. Burke, and W. Harrington. 1974. Cooperative role of two sulfhydryl groups in myosin adenosine triphosphatase. Biochemistry 13:2014-2022.

49. Thomas, D. D., J. C. Seidel, J. S. Hyde, and J. Gergely. 1975. Motion of subfragment-1 in myosin and its supramolecular complexes: saturation transfer electron paramagnetic resonance. Proc Natl Acad Sci U S A 72:1729-1733.

50. Thomas, D. D. 1977. Saturation transfer EPR. Trends Biochem Sci 2:N62-N63.

51. Thomas, D. D., L. R. Dalton, and J. S. Hyde. 1976. Rotational diffusion studied by passage saturation transfer electron paramagnetic resonance. J Chem Phys 65.

52. Howard, E. C., K. M. Lindahl, C. F. Polnaszek, and D. D. Thomas. 1993. Simulation of saturation transfer electron paramagnetic resonance spectra for rotational motion with restricted angular amplitude. Biophys J 64:581-593.

53. Svensson, E. C. and D. D. Thomas. 1986. ATP induces microsecond rotational motions of myosin heads crosslinked to actin. Biophys J 50:999-1002.

54. Barnett, V. A. and D. D. Thomas. 1989. Microsecond rotational motion of spin-labeled myosin heads during isometric muscle contraction. Saturation transfer electron paramagnetic resonance. Biophys J 56:517-523.

55. Nitao, L. K., T. O. Yeates, and E. Reisler. 2002. Conformational dynamics of the SH1-SH2 helix in the transition states of myosin subfragment-1. Biophys J 83:2733-2741.

56. Flicker, P. F., R. A. Milligan, and D. Applegate. 1991. Cryo-electron microscopy of S1-decorated actin filaments. Adv Biophys 27:185-196.

57. Moore, P. B., H. E. Huxley, and D. J. DeRosier. 1970. Three-dimensional reconstruction of F-actin, thin filaments and decorated thin filaments. J Mol Biol 50:279-295.

58. Fajer, P. G., E. A. Fajer, M. Schoenberg, and D. D. Thomas. 1991. Orientational disorder and motion of weakly attached cross-bridges. Biophys J 60:642-649.

59. Raucher, D. and P. G. Fajer. 1994. Orientation and dynamics of myosin heads in aluminum fluoride induced pre-power stroke states: an EPR study. Biochemistry 33:11993-11999.

60. Agafonov, R. V., Y. E. Nesmelov, M. A. Titus, and D. D. Thomas. 2008. Muscle and nonmuscle myosins probed by a spin label at equivalent sites in the force-generating domain. Proc Natl Acad Sci U S A 105:13397-13402.

61. Liang, W. and J. A. Spudich. 1998. Nucleotide-dependent conformational change near the fulcrum region in Dictyostelium myosin II. Proc Natl Acad Sci U S A 95:12844-12847.

62. Bobkov, A. A., K. Sutoh, and E. Reisler. 1997. Nucleotide and actin binding properties of the isolated motor domain from Dictyostelium discoideum myosin. J Muscle Res Cell Motil 18:563-571.

63. Agafonov, R. V., M. A. Titus, Y. E. Nesmelov, and D. D. Thomas. 2008. Muscle and Nonmuscle Myosins Probed by a Spin Label at Equivalent Sites in the Force-Generating Domain. Proc Natl Acad Sci U S A:submitted.

64. Volkmann, N., H. Lui, L. Hazelwood, K. M. Trybus, S. Lowey, and D. Hanein. 2007. The R403Q myosin mutation implicated in familial hypertrophic cardiomyopathy causes disorder at the actomyosin interface. PLoS ONE 2:e1123.

65. Seidman, J. G. and C. Seidman. 2001. The genetic basis for cardiomyopathy: from mutation identification to mechanistic paradigms. Cell 104:557-567.

66. Rayment, I., H. M. Holden, J. R. Sellers, L. Fananapazir, and N. D. Epstein. 1995. Structural interpretation of the mutations in the beta-cardiac myosin that have been implicated in familial hypertrophic cardiomyopathy. Proc Natl Acad Sci U S A 92:3864-3868.

67. Sasaki, N., R. Ohkura, and K. Sutoh. 2002. Dictyostelium myosin II as a model to study the actin-myosin interactions during force generation. J Muscle Res Cell Motil 23:697-702.

68. Fujita, H., S. Sugiura, S. Momomura, M. Omata, H. Sugi, and K. Sutoh. 1997. Characterization of mutant myosins of Dictyostelium discoideum equivalent to human familial hypertrophic cardiomyopathy mutants. Molecular force level of mutant myosins may have a prognostic implication. J Clin Invest 99:1010-1015.

69. Liu, X., S. Shu, M. Kovacs, and E. D. Korn. 2005. Biological, biochemical, and kinetic effects of mutations of the cardiomyopathy loop of Dictyostelium myosin II: importance of ALA400. J Biol Chem 280:26974-26983.

70. Sweeney, H. L., A. J. Straceski, L. A. Leinwand, B. A. Tikunov, and L. Faust. 1994. Heterologous expression of a cardiomyopathic myosin that is defective in its actin interaction. J Biol Chem 269:1603-1605.

71. Roopnarine, O. and L. A. Leinwand. 1998. Functional analysis of myosin mutations that cause familial hypertrophic cardiomyopathy. Biophys J 75:3023-3030.

72. Yamashita, H., M. J. Tyska, D. M. Warshaw, S. Lowey, and K. M. Trybus. 2000. Functional consequences of mutations in the smooth muscle myosin heavy chain at sites implicated in familial hypertrophic cardiomyopathy. J Biol Chem 275:28045-28052.

73. Palmiter, K. A., M. J. Tyska, J. R. Haeberle, N. R. Alpert, L. Fananapazir, and D. M. Warshaw. 2000. R403Q and L908V mutant beta-cardiac myosin from patients with familial hypertrophic cardiomyopathy exhibit enhanced mechanical performance at the single molecule level. J Muscle Res Cell Motil 21:609-620.

74. Liu, Y., M. Scolari, W. Im, and H. J. Woo. 2006. Protein-protein interactions in actin-myosin binding and structural effects of R405Q mutation: a molecular dynamics study. Proteins 64:156-166.

75. Mendelson, R. and E. P. Morris. 1997. The structure of the acto-myosin subfragment 1 complex: results of searches using data from electron microscopy and x-ray crystallography. Proc Natl Acad Sci U S A 94:8533-8538.

76. Rayment, I., H. M. Holden, M. Whittaker, C. B. Yohn, M. Lorenz, K. C. Holmes, and R. A. Milligan. 1993. Structure of the actin-myosin complex and its implications for muscle contraction. Science 261:58-65.

77. Schroder, R. R., D. J. Manstein, W. Jahn, H. Holden, I. Rayment, K. C. Holmes, and J. A. Spudich. 1993. Three-dimensional atomic model of F-actin decorated with Dictyostelium myosin S1. Nature 364:171-174.

78. Volkmann, N., G. Ouyang, K. M. Trybus, D. J. DeRosier, S. Lowey, and D. Hanein. 2003. Myosin isoforms show unique conformations in the actin-bound state. Proc Natl Acad Sci U S A 100:3227-3232.

79. Klein, J. C., A. R. Burr, B. Svensson, D. J. Kennedy, J. Allingham, M. A. Titus, I. Rayment, and D. D. Thomas. 2008. Actin-binding cleft closure in myosin II probed by site-directed spin labeling and pulsed EPR. Proc Natl Acad Sci U S A 105:12867-12872.

80. Volkmann, N., D. Hanein, G. Ouyang, K. M. Trybus, D. J. DeRosier, and S. Lowey. 2000. Evidence for cleft closure in actomyosin upon ADP release. Nat Struct Biol 7:1147-1155.

81. Gulick, A. M., C. B. Bauer, J. B. Thoden, and I. Rayment. 1997. X-ray structures of the MgADP, MgATPgammaS, and MgAMPPNP complexes of the Dictyostelium discoideum myosin motor domain. Biochemistry 36:11619-11628.

82. Reubold, T. F., S. Eschenburg, A. Becker, F. J. Kull, and D. J. Manstein. 2003. A structural model for actin-induced nucleotide release in myosin. Nat Struct Biol 10:826-830.